

RESEARCH ARTICLE

10.1002/2014JD022428

Key Points:

- JEM-GLIMS started continuous nadir observations of lightning and TLEs from ISS
- Optical instruments succeeded in characterizing lightning and TLE emissions
- Properties of lightning discharges exciting VHF pulses were first identified

Correspondence to:

M. Sato,
msato@ep.sci.hokudai.ac.jp

Citation:

Sato, M., et al. (2015), Overview and early results of the Global Lightning and Sprite Measurements mission, *J. Geophys. Res. Atmos.*, 120, 3822–3851, doi:10.1002/2014JD022428.

Received 11 AUG 2014

Accepted 27 MAR 2015

Accepted article online 23 APR 2015

Published online 11 MAY 2015

Overview and early results of the Global Lightning and Sprite Measurements mission

M. Sato¹, T. Ushio², T. Morimoto³, M. Kikuchi⁴, H. Kikuchi², T. Adachi⁵, M. Suzuki⁶, A. Yamazaki⁶, Y. Takahashi¹, U. Inan⁷, I. Linscott⁷, R. Ishida⁸, Y. Sakamoto⁹, K. Yoshida⁹, Y. Hobara¹⁰, T. Sano⁶, T. Abe⁶, M. Nakamura⁶, H. Oda¹¹, and Z.-I. Kawasaki²

¹Faculty of Science, Hokkaido University, Sapporo, Japan, ²Faculty of Engineering, Osaka University, Suita, Japan, ³Faculty of Science and Engineering, Kinki University, Higashiosaka, Japan, ⁴National Institute of Polar Research, Tachikawa, Japan, ⁵Meteorological Research Institute, Japan Meteorological Agency, Tsukuba, Japan, ⁶Institute of Space and Astronautical Science, JAXA, Sagami-hara, Japan, ⁷Department of Electrical Engineering, Stanford University, Stanford, California, USA, ⁸Faculty of Engineering, Osaka Prefecture University, Sakai, Japan, ⁹Department of Engineering, Tohoku University, Sendai, Japan, ¹⁰Faculty of Informatics and Engineering, University of Electro-Communications, Chofu, Japan, ¹¹Human Spaceflight Mission Directorate, JAXA, Tsukuba, Japan

Abstract Global Lightning and Sprite Measurements on Japanese Experiment Module (JEM-GLIMS) is a space mission to conduct the nadir observations of lightning discharges and transient luminous events (TLEs). The main objectives of this mission are to identify the horizontal distribution of TLEs and to solve the occurrence conditions determining the spatial distribution. JEM-GLIMS was successfully launched and started continuous nadir observations in 2012. The global distribution of the detected lightning events shows that most of the events occurred over continental regions in the local summer hemisphere. In some events, strong far-ultraviolet emissions have been simultaneously detected with N₂ 1P and 2P emissions by the spectrophotometers, which strongly suggest the occurrence of TLEs. Especially, in some of these events, no significant optical emission was measured by the narrowband filter camera, which suggests the occurrence of elves, not sprites. The VLF receiver also succeeded in detecting lightning whistlers, which show clear falling-tone frequency dispersion. Based on the optical data, the time delay from the detected lightning emission to the whistlers was identified as ~10 ms, which can be reasonably explained by the wave propagation with the group velocity of whistlers. The VHF interferometer conducted the spaceborne interferometric observations and succeeded in detecting VHF pulses. We observed that the VHF pulses are likely to be excited by the lightning discharge possibly related with in-cloud discharges and measured with the JEM-GLIMS optical instruments. Thus, JEM-GLIMS provides the first full set of optical and electromagnetic data of lightning and TLEs obtained by nadir observations from space.

1. Introduction

About 25 years ago, transient optical flashes occurring above an active thundercloud were first discovered by Franz *et al.* [1990] and named transient luminous events (TLEs). TLEs have been found to occur in the stratosphere and mesosphere and that they are always associated with strong lightning discharges [Boccippio *et al.*, 1995; Lyons, 1996]. So far, numerous ground-based optical and radio observations and theoretical studies using numerical simulation techniques have been intensively performed [Sentman *et al.*, 1995; Fukunishi *et al.*, 1996; Wescott *et al.*, 1995; Pasko *et al.*, 1997, 2002; Su *et al.*, 2003; Marshall *et al.*, 2010, and references therein]. Sprites excited by intense positive cloud-to-ground (+CG) discharges are one of the occurrence types of TLEs and are the most frequently observed events by ground-based optical observations. Although the well-accepted generation mechanism for sprites is the quasi-electrostatic field model [Pasko *et al.*, 1997], a number of observational facts that cannot be explained only by this model have been reported, such as the number of sprite columns, the displacement between the sprite location and the location of the parent CG discharge, the time delay from the occurrence of the parent CG discharge, the differences between occurrence types (i.e., columniform and carrot sprites), and the horizontal distributions of sprites [Wescott *et al.*, 2001; Bell *et al.*, 1998; Cummer and Füllekrug, 2001]. All these properties are linked with the occurrence conditions of sprites.

Recent studies of sprites, however, have provided some hints to solve the occurrence conditions. For the number of sprite columns, Adachi *et al.* [2004] showed a clear proportional relation between the number of

sprite columns and the peak current intensity of the parent CG discharge. Based on optical and very low frequency (VLF) wave observations, *Ohkubo et al.* [2005] found a cluster of weak VLF pulses occurring just before the sprite appearance. These facts imply that electromagnetic pulses (EMPs) are emitted not only by the return stroke current but also by the in-cloud discharge currents. Such pulses may be essential in determining the number of sprite columns. For the horizontal displacement between the sprite location and the location of the parent CG discharge, *Lyons*, 1996] statistically analyzed sprite image and lightning data obtained by the National Lightning Detection Network and found that sprites sometimes appear with a maximum horizontal shift of 50 km. *Lu et al.* [2009, 2013] analyzed the optical data of sprites and the Lightning Mapping Array (LMA) data and compared the sprite occurrence location with three-dimensional in-cloud leader structures and the return stroke point of the parent CG discharge. It was shown that the central region where the positive charges are neutralized in the thundercloud is not always equal to the return stroke point and that the large-scale structure of sprites could be affected by the in-cloud geometry of charge removal. For analyzing the time delay of the parent CG discharges and the differences among the occurrence types of sprites, recent quantitative data analyses, using ground-based optical data, electromagnetic waveform data, and data from the modeling of the electric field at the sprite altitude calculated by the finite difference time-domain method, revealed that the shape of the charge moment change (CMC) waveform and the impulse CMC, which is defined as the total charge moment change over the first 2 ms of the lightning stroke, are important in characterizing these aspects [*Cummer and Lyons*, 2005; *Hu et al.*, 2007; *Li et al.*, 2008; *Gamerota et al.*, 2011; *Lang et al.*, 2011]. Using optical data obtained by the Imager of Sprites and Upper Atmospheric Lightning (ISUAL) onboard the FORMOSAT-2 satellite, *Adachi et al.* [2008] reported that the difference in CMC development of the sprite-producing CG discharges can determine the appearance of a sprite halo and/or sprite streamers. A recent report by *Qin et al.* [2013] showed that the difference in CMC time variations could determine the occurrence of columniform or carrot sprites. All these results imply that the time variation of CMC development and the resultant electric field changes at the sprite altitude may have a direct influence on determining the time delay and the occurrence type.

In contrast, the physical parameters determining the horizontal distributions of sprites are not well understood. Although it is suggested that the inhomogeneity in the electron density at 80–90 km altitudes may have a direct impact on the horizontal distribution of sprites and the formation of sprite streamers [*Qin et al.*, 2011], there are many factors that can create such inhomogeneity, such as, atmospheric gravity waves, micrometeors, interference of EMPs emitted by in-cloud lightning currents. In previous studies, the relation between sprite formation and the distribution of OH airglow emissions and the relation between the circular organization of columniform sprite elements and the charge center of the parent CG discharges in thunderclouds were introduced [*Sentman et al.*, 2003; *Yair et al.*, 2009; *Vadislavsky et al.*, 2009]. However, detailed two- or three-dimensional distributions of sprites were not estimated in these studies, perhaps due to the difficulties of triangulation analysis. Thus, to clarify the occurrence conditions that determine the appearance of sprite elements, an observational identification of the horizontal distribution of sprites is essential. As geographical and meteorological conditions strictly limit the feasibility of simultaneous measurements of sprites from multiple ground-based observation sites, it is quite useful to conduct nadir observations of lightning and sprites from space. Based on this science scope, nadir observations of sprites were once conducted from the International Space Station (ISS) using wideband and narrowband CCD cameras [*Blanc et al.*, 2004]. The time accuracy of the recorded lightning and possible sprite events was approximately ± 1 s [*Blanc et al.*, 2004]. Thus, it was difficult to validate the parent CG discharges of the possible sprite events reported in that study using ground-based extremely low frequency (ELF) and VLF measurement data. Recently, optical observations of TLEs were also conducted from the ISS [*Jehl et al.*, 2013; *Yair et al.*, 2013]. *Jehl et al.* [2013] analyzed 15 sprite events detected using a Nikon digital color camera from the ISS, and they showed that the measured optical emissions of sprites mainly originated in the N_2 1P band system. *Yair et al.* [2013] analyzed image data obtained by an EMCCD normal video rate color TV camera installed at the Cupola module at the ISS and showed the first color nadir images of sprites. These results suggest that the ISS is one of the best platforms to conduct TLE observations from space.

Using the optical data obtained by ISUAL on board the FORMOSAT-2 satellite, the global occurrence rates and distributions for the major types of TLEs were estimated [*Chen et al.*, 2008]. The occurrence rates of elves, sprites, halos, and gigantic jets are reported to be 3.23, 0.50, 0.39, and 0.01 events/min, respectively. Although the first detailed global occurrence rates were revealed in this study, these numbers were derived from measurements of the lightning and TLE activities at ~ 24 LT due to the Sun-synchronized polar orbit of the

satellite. As lightning activity peaks at ~16–17 LT in general [Mackerras and Darveniza, 1994; Liu and Zipser, 2008], these occurrence rates naturally contain large estimation errors. The authors pointed out that the corrected global occurrence rates for sprites and elves taking the instrumental detection sensitivity and the restricted survey area into account are likely to be larger by a factor of 2 and an order of magnitude, respectively [Chen *et al.*, 2008]. Based on space shuttle observations of TLEs, Yair *et al.* [2004] estimated the occurrence rate of sprites to be 0.13 events/min. Sato and Fukunishi [2003] analyzed ELF magnetic field waveform data and estimated the global occurrence rate of sprites by picking up ~715,500 transient Schumann resonance events and by calculating the CMC value of each intense CG discharge. They reported that the rate was estimated to be 0.5 events/min, which is similar to the number derived from ISUAL data analysis. However, in such ELF data analysis, the global occurrence rate was estimated by integrating the occurrence probability of sprites determined by the CMC value of each intense CG discharge. Thus, the estimated global occurrence rate of sprites in their study was simply the global occurrence “probability.” Greenberg *et al.* [2007] analyzed ELF signals excited by both TLEs and non-TLEs producing CG discharges and showed that even CG discharges having high CMC values do not necessarily produce sprites. This fact implies that the global occurrence rates of TLEs may actually be much lower than the rates deduced by Sato and Fukunishi [2003]. Ignaccolo *et al.* [2006] introduced a new formula to calculate the planetary rate of sprites and estimated the average rate to be ~2.8 events/min with an accuracy of a factor ~2–3, which is one order larger than the values in Chen *et al.* [2008], Yair *et al.* [2004], and Sato and Fukunishi [2003]. To obtain the more accurate global occurrence rates and distributions of TLEs, it is essential to conduct the optical observations from space by scanning all the local time regions, such as, the MicroLab-1/Optical Transient Detector (OTD) and Tropical Rainfall Measuring Mission/Lightning Imaging Sensor (TRMM/LIS) measurements. This will contribute to estimates of the amount of NO_x, HO_x, and O_x produced or depleted by TLEs on the global scale and will help in understanding the possible chemical impact of TLEs on Earth’s atmosphere [Hiraki *et al.*, 2008; Sentman *et al.*, 2008].

For the lightning observations from space, the MicroLab-1/OTD and TRMM/LIS missions brought new knowledge about the global occurrence rates and distributions of lightning discharges [Boccippio *et al.*, 2000; Christian *et al.*, 2003; Cecil *et al.*, 2014]. In these satellite missions, the nadir observations of lightning emissions using a CCD camera equipped with narrowband optical filter at 777.4 nm were conducted, which enabled lightning emissions both on the nightside and dayside to be measured. From these measurements, the morphology of the lightning emissions was revealed. Furthermore, it was found that lightning discharges mainly occur over continental regions and that the global occurrence rate is ~50 flash/s. Note that most of the lightning events detected by TRMM/LIS originated from intracloud (IC) discharges or the subsequent stroke of a return stroke [Thomas *et al.*, 2000; Ushio *et al.*, 2002]. Thus, it is difficult to distinguish the optical emissions of CG discharges from those of IC discharges and estimate the latitudinal variations of the IC/CG ratio denoted by Z only from the TRMM/LIS optical data. In general, at the equatorial and near equatorial zone, the base altitude of thunderclouds tend to be low, and the main negative charge area tends to be high, which leads the generation of IC discharges more frequently [Mushtak *et al.*, 2005]. On the other hand, at mid-latitudes, the cloud base tend to be at high altitudes, and the negative charge tend to be at low altitudes, which leads the generation of CG discharges [Mushtak *et al.*, 2005]. These tendencies can be confirmed by the latitudinal dependences of Z values, that is, $Z = \sim 6 - 9$ in the equatorial region and $Z < 4$ in the latitudinal range over 30° [Prentice and Mackerras, 1977; Mackerras and Darveniza, 1994; Mackerras *et al.*, 1998; Boccippio *et al.*, 2001]. However, such an IC/CG ratio was calculated using ground-based lightning data obtained at limited and specific areas, and the latitudinal variations of Z seems to contain large errors, as shown in Figure 1 in Boccippio *et al.* [2001]. Thus, the understanding of Z variations at the planetary scale gradually progressed. To estimate more accurate Z variations and to identify the relation to the cloud climatology, it is useful to carry out spectral measurements of lightning emissions from a space platform where the lightning activities at all local time regions can be scanned. This will substantially contribute to the estimates of regional and global NO_x production and the assessments of lightning effects on the global electric circuit [Boccippio *et al.*, 2001].

As described above, the scientific importance of conducting nadir observations of lightning and TLEs from a space platform that realizes scanning measurements over all local time areas is summarized as follows: (1) the detection of the detailed horizontal distribution of sprites, (2) identification of the occurrence conditions that determine the horizontal distribution of sprites, (3) estimation of the quantitative global occurrence rates and distributions of lightning and TLEs and their seasonal variations and LT dependences, and (4) quantitative estimation of Z variations at the planetary scale based on imaging and spectrophotometric measurements of lightning emissions. To address these scientific objectives, a space mission, named the Global Lightning

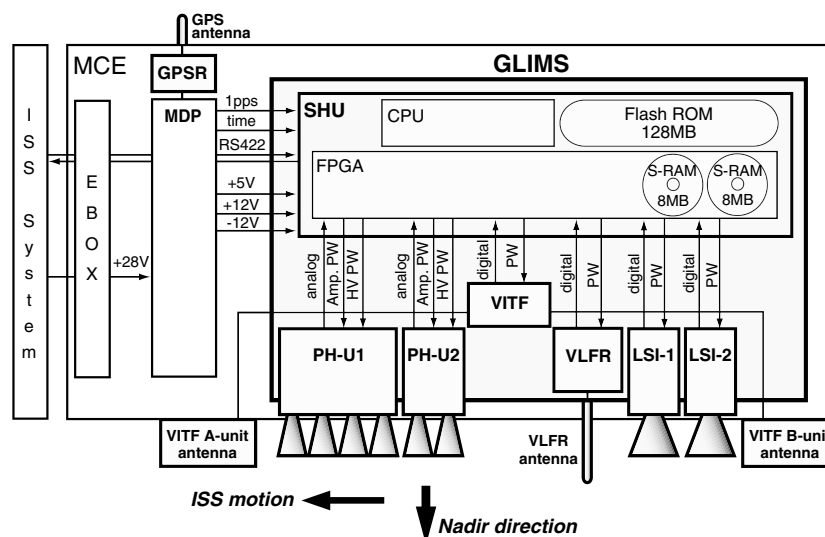


Figure 1. Schematic showing the construction of JEM-GLIMS instruments and the interface structure between JEM-GLIMS and the upper level subsystems. All JEM-GLIMS instruments are installed on the nadir-directing base plate of MCE.

and Sprite Measurements on Japanese Experiment Module (JEM-GLIMS), to conduct the nadir observations of lightning and TLEs from the JEM Exposed Facility (EF) on board the ISS was planned in 2007 [Ushio *et al.*, 2011]. The most outstanding point of this mission is that both optical instruments and electromagnetic wave receivers are employed not only to characterize the spatiotemporal changes of the lightning and TLE emissions but also to identify the electrical properties of lightning discharges and parent lightning discharges of TLEs. Thus, JEM-GLIMS has conducted the first comprehensive nadir observations of lightning and TLEs with these optical and electromagnetic instruments.

Here we report an overview of the JEM-GLIMS mission and the early results derived from JEM-GLIMS optical and electromagnetic observations and discuss the expected science outputs. JEM-GLIMS science instruments and their specifications and the observation method are introduced in section 2. The global distribution of the detected lightning events and their seasonal variations are presented in section 3. Examples of CG and IC events and lightning events accompanied by strong far-ultraviolet (FUV) emissions are introduced in sections 4 and 5. In section 6, the examples of electromagnetic waves detected by JEM-GLIMS electromagnetic wave receivers are shown. Finally, the conclusions of this report are presented in section 7.

2. JEM-GLIMS Mission

2.1. JEM-GLIMS Instruments and System Configuration

The overall system configuration of JEM-GLIMS instruments and the interface structure of the upper level subsystems is shown in Figure 1. JEM-GLIMS comprises two optical instruments, two electromagnetic wave receivers, and an onboard computer. For the optical instruments, two Complementary Metal Oxide Semiconductor (CMOS) cameras (LSI: Lightning and Sprite Imager) [Sato *et al.*, 2011a] and six-channel spectrophotometers (PH: Photometer) [Sato *et al.*, 2011b] are employed. For the electromagnetic wave receivers, two sets of very high frequency (VHF) wave receivers (VITF: VHF Interferometer) [Morimoto *et al.*, 2011] and a VLF wave receiver (VLFR: VLF Receiver) are adopted. All these science instruments are controlled by the onboard computer (SHU: Science Instrument Handling Unit) [M. Kikuchi *et al.*, 2011]. SHU is electrically and functionally connected to the ISS main system through the upper level subsystems (Mission Data Processor (MDP) and Electronics Box (EBOX)). Note that all the science instruments are installed on the base plate of the bus system, and the LSI optics, PH optics, VLFR antenna, and VITF antennas are directly exposed to space in the nadir direction.

The main purpose of LSI is to detect the shape of the optical emissions from lightning and TLEs and measure their spatiotemporal changes [Sato *et al.*, 2011a]. LSI uses a CMOS sensor (STAR250) as an imaging device and is composed of two cameras, denoted as LSI-1 and LSI-2. The detailed specifications of LSI-1 and LSI-2 are presented in Table 1. A wideband optical filter transmitting 768–830 nm emissions is mounted on top of the

Table 1. Specification of LSI

	LSI-1	LSI-2
Target	OI (777 nm), NI (822 nm)	N ₂ 1P _(3,1)
Passband (FWHM ^a)	768–830 nm	760–775 nm
Pixel number	512 × 512	
FOV	28.3° × 28.3°	
Spatial resolution	400 m × 400 m at ground surface 320 m × 320 m at 80 km altitude	
Time resolution	32.8 ms (nominal)	
Sensitivity	0.1 A/W	
Resolution	10 bit	
Image capturing	4 images/event (nominal)	

^aFWHM = full width at half maximum.

LSI-1 lens, while a narrowband filter transmitting 760–775 nm emissions is mounted on top of the LSI-2 lens. The same kind of filter choice was performed by *Blanc et al.* [2004], who conducted campaign-based nadir observations of TLEs from the ISS. The transmission curves of LSI filters are plotted in Figure 2. In this figure, the solid lines correspond to the transmittance of LSI-1 and LSI-2 filters in the 720–860 nm wavelength range, and the red-colored solid line corresponds to the modeled atmospheric transmittance calculated by assuming that the light source is located at 8 km altitude and that the photons from the light source propagate in the zenith direction. In the wavelength range

of the LSI-1 filter, there are lightning emissions from OI (777.4 nm), OI (794.7 nm), and NI (820.0 nm) and TLE emissions from N₂ 1P(2,0) (775.4 nm) and N₂ 1P(6,5) (804.7 nm) [Orville and Henderson, 1984; Bucseles et al., 2003; Gordillo-Vázquez et al., 2011]. As lightning emissions are much stronger than TLE emissions in this wavelength range, LSI-1 mainly measures lightning emissions. On the other hand, in the wavelength range of the LSI-2 filter, there are the continuum component of lightning emissions and TLE emissions of N₂ 1P(3,1) (762.7 nm). As shown by the red-colored line in Figure 2, the continuum lightning emissions are absorbed by O₂ molecules in the atmosphere when traveling from the lower altitude where lightning discharges occur to the ISS. Thus, LSI-2 mainly measures TLE emissions. By subtracting the appropriately scaled LSI-1 image data from the LSI-2 image data, it is possible to selectively extract only the TLE emissions, which is first introduced by *Blanc et al.* [2004]. The field of view (FOV) of LSI is 28.3° × 28.3°, which corresponds to a spatial resolution of 400 m/pixel at the ground level and 320 m/pixel at 80 km altitude. The time resolution is 32.8 ms, and the resolution of the image data is 10 bit.

To obtain the light curve data and to estimate the absolute intensity of lightning and TLE emissions, six-channel spectrophotometers denoted as PH are employed [Sato et al., 2011b]. The detailed specification of PH is given in Table 2. PH comprises six photometers (denoted by PH1–PH6) and is used to detect the N₂ and N₂⁺ emissions of lightning and TLEs. Summaries of the transmission curves of PH optical filters are presented in Figure 3. Solid lines in Figures 3a and 3b are the transmittance of the PH optical filters and the thin blue-colored line in Figure 3a and the red-colored line in Figure 3b are the modeled atmospheric transmittances calculated by the same assumption used for Figure 2. PH1 measures FUV emissions in the 150–280 nm wavelength range, and FUV emissions come from the N₂ Lyman-Birge-Hopfield (LBH) band system. PH1 is

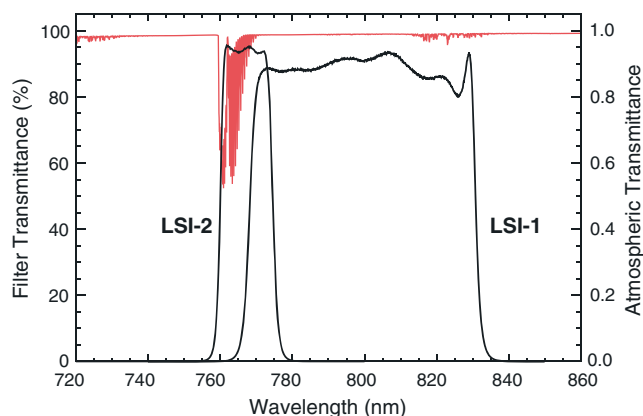


Figure 2. Transmittance of the optical filters for LSI-1 and LSI-2. The red-colored line corresponds to the modeled atmospheric transmittance assuming that the light source is located at 8 km altitude and that the optical emissions propagate in the zenith direction.

the same type of the photometer as the ISUAL Spectral Photometer on board the FORMOSAT-2 satellite, and this channel is essentially effective for the identification of TLE occurrence [Kuo et al., 2005a, 2007; Chang et al., 2010]. PH2 and PH5 measure optical emissions in the wavelength range of 332–342 nm and 310–321 nm, where the optical emissions of N₂ 2P(0,0) (337.0 nm) and N₂ 2P(1,0) (315.8 nm) exist, respectively. PH3 measures optical emissions in the 755–766 nm wavelength range and is used to detect the N₂ 1P(3,1) (762.7 nm) emissions. PH4 also measures the N₂ 1P emissions, but this channel is equipped with a wideband optical filter transmitting the 599–900 nm emissions and is mainly used to detect lightning

Table 2. Specification of PH

	PH1	PH2	PH3	PH4	PH5	PH6
Target	N ₂ LBH	N ₂ 2P _(0,0)	N ₂ 1P _(3,1)	N ₂ 1P	N ₂ 2P _(1,0)	N ₂ ⁺ 1N _(0,0)
Passband (FWHM)	150–280 nm	332–342 nm	755–766 nm	599–900 nm	310–321 nm	386–397 nm
FOV		42.7°		86.8°		42.7°
Sampling rate	20 kHz					
Sensitivity (W/m ²)	1.8 × 10 ⁻⁹	2.4 × 10 ⁻⁷	1.7 × 10 ⁻⁶	1.3 × 10 ⁻⁶	9.7 × 10 ⁻¹¹	1.6 × 10 ⁻⁷
Resolution	12 bit					
Data length	512 ms					

emissions. PH6 measures the optical emissions of N₂⁺ 1N(0,0) (391.4 nm) and uses an optical filter transmitting the 386–397 nm emissions. PH1–3, PH5, and PH6 have a conical FOV of 42.7°, which is nearly equal to the circumscribed circle of the LSI FOV. In contrast, PH4 has a conical FOV of 86.8° so that it can detect parent lightning discharges that generate terrestrial gamma ray flashes. The light curve data of all PH channels are recorded with a sampling frequency of 20 kHz (= 50 μs time resolution) and a 12 bit resolution. As shown schematically in Figure 1, PH1–4 are installed in the “Unit-1” housing box (PH-U1), while PH5 and PH6 are installed in the “Unit-2” housing box (PH-U2).

Electromagnetic waves in the VLF range are excited by lightning discharges and are reflected from the ionosphere. However, some VLF waves penetrate into the ionosphere and magnetosphere as lightning

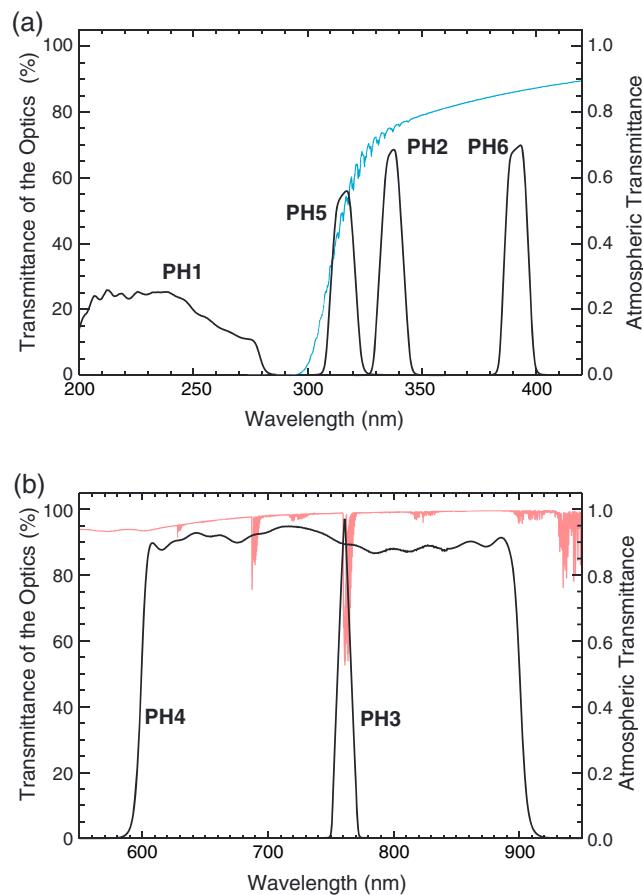


Figure 3. (a) Transmittance of the PH1, PH2, PH5, and PH6 optical filters. (b) Same as Figure 3a except for the PH3 and PH4 optical filters. Blue-colored line in Figure 3a and red-colored line in Figure 3b are the modeled atmospheric transmittances assuming that the light source is located at 8 km altitude and the optical emissions propagate in the zenith direction.

Table 3. Specification of VLFR

Antenna Type	15 cm Monopole Antenna
Antenna directivity	2π rad
Bandwidth	1–30 kHz
Sampling frequency	100 kHz
Sensitivity	32.6 $\mu\text{V}/\text{m}/\text{LSB}^{\text{a}}$
Resolution	14 bit
Data length	512 ms/event

^aLSB = least significant bit.

(C/NOFS) satellite launched in 2008 also detected large quantities of whistler events [Holzworth *et al.*, 2011; Jacobson *et al.*, 2011]. The detailed comparison between the VEFI data and the ground-based World Wide Lightning Location Network (WWLLN) data reveals the propagation characteristics of the whistler waves and the related ionospheric disturbances. To detect lightning-excited whistlers and identify the relation between the parent lightning discharges and the occurrence of TLEs, one component of the VLF receiver denoted as VLFR is employed for the JEM-GLIMS mission. The detailed specification of VLFR is summarized in Table 3. For this receiver system, a 15 cm monopole antenna directed in the nadir direction is used and attached to the base plate of the bus system. Thus, the directivity of the antenna becomes 2π rad. The VLFR frequency range is 1–30 kHz, and the sampling frequency is 100 kHz with a 14 bit resolution.

Impulsive electromagnetic waves in the VHF range are usually emitted from the tips of the leader development in thunderclouds. By simultaneously measuring these VHF pulses at multiple ground stations, the source locations in the thundercloud can be estimated using interferometry techniques [Rison *et al.*, 1999; Morimoto *et al.*, 2005; Lu *et al.*, 2009]. As such impulsive VHF waves can penetrate into the ionosphere and magnetosphere, these VHF pulses can be detected at the satellite altitude and were actually measured by the FORTE and Mado-1 satellites [Suszcynsky *et al.*, 2000; H. Kikuchi *et al.*, 2011, 2013]. On these spacecraft, only one component of the VHF antenna was installed, so it was not possible to geolocate the source position of the VHF pulses using these satellite data. In the JEM-GLIMS mission, two components of the VHF receivers, denoted as VITF, are employed to identify the spatiotemporal development of the in-cloud currents of the CG discharges exciting TLEs [Morimoto *et al.*, 2011]. The detailed specification of VITF is summarized in Table 4. Two patch-type antennas are installed on the base plate of the bus system, separated from each other by a 1.6 m interval, and directed in the nadir direction. Then, these two antennas can work as an interferometer. Directivity of the antenna is 2π rad, and the frequency range of the receiver is 70–100 MHz. Waveform data of VHF pulses are digitally sampled at a 200 MHz sampling frequency with an 8 bit resolution. When the amplitude of a VHF pulse exceeds the trigger threshold level, the waveform data at time intervals of 2.56 μs are stored in the onboard ring-buffer memory in the VITF electronics, which can store a total of 130 pulse data at maximum.

SHU is the onboard computer controlling all the science instruments [M. Kikuchi *et al.*, 2011]. It controls the power of each science instrument, event triggering, data acquisition, data compression, and data processing for the command and telemetry communication. There is another onboard computer, named the Mission

Table 4. Specification of VITF

Antenna Type	Patch-Type Antenna
Number of antenna	2
Antenna directivity	2π rad
Bandwidth	70–100 MHz
Sampling frequency	200 MHz
Sensitivity	$\sim 90 \mu\text{V}/\text{m}/\text{LSB}$
Resolution	8 bit
Data length	130 pulses/event (max.) 2.5 $\mu\text{s}/\text{pulse}$

whistlers and are detected by satellites. A French microsatellite named Detection of Electromagnetic Emissions Transmitted from Earthquake Regions (DEMETER) succeeded in detecting such lightning whistlers and showed clear observational evidence of the electromagnetic energy input from the lower atmosphere to the upper atmosphere by lightning discharges [Lefeuvre *et al.*, 2009; Chum *et al.*, 2009; Fiser *et al.*, 2010; Parrot *et al.*, 2013]. The Vector Electric Field Instrument (VEFI) on board the Communication/Navigation Outage Forecast System

(C/NOFS) satellite launched in 2008 also detected large quantities of whistler events [Holzworth *et al.*, 2011; Jacobson *et al.*, 2011]. The detailed comparison between the VEFI data and the ground-based World Wide Lightning Location Network (WWLLN) data reveals the propagation characteristics of the whistler waves and the related ionospheric disturbances. To detect lightning-excited whistlers and identify the relation between the parent lightning discharges and the occurrence of TLEs, one component of the VLF receiver denoted as VLFR is employed for the JEM-GLIMS mission. The detailed specification of VLFR is summarized in Table 3. For this receiver system, a 15 cm monopole antenna directed in the nadir direction is used and attached to the base plate of the bus system. Thus, the directivity of the antenna becomes 2π rad. The VLFR frequency range is 1–30 kHz, and the sampling frequency is 100 kHz with a 14 bit resolution.

Impulsive electromagnetic waves in the VHF range are usually emitted from the tips of the leader development in thunderclouds. By simultaneously measuring these VHF pulses at multiple ground stations, the source locations in the thundercloud can be estimated using interferometry techniques [Rison *et al.*, 1999; Morimoto *et al.*, 2005; Lu *et al.*, 2009]. As such impulsive VHF waves can penetrate into the ionosphere and magnetosphere, these VHF pulses can be detected at the satellite altitude and were actually measured by the FORTE and Mado-1 satellites [Suszcynsky *et al.*, 2000; H. Kikuchi *et al.*, 2011, 2013]. On these spacecraft, only one component of the VHF antenna was installed, so it was not possible to geolocate the source position of the VHF pulses using these satellite data. In the JEM-GLIMS mission, two components of the VHF receivers, denoted as VITF, are employed to identify the spatiotemporal development of the in-cloud currents of the CG discharges exciting TLEs [Morimoto *et al.*, 2011]. The detailed specification of VITF is summarized in Table 4. Two patch-type antennas are installed on the base plate of the bus system, separated from each other by a 1.6 m interval, and directed in the nadir direction. Then, these two antennas can work as an interferometer. Directivity of the antenna is 2π rad, and the frequency range of the receiver is 70–100 MHz. Waveform data of VHF pulses are digitally sampled at a 200 MHz sampling frequency with an 8 bit resolution. When the amplitude of a VHF pulse exceeds the trigger threshold level, the waveform data at time intervals of 2.56 μs are stored in the onboard ring-buffer memory in the VITF electronics, which can store a total of 130 pulse data at maximum.

SHU is the onboard computer controlling all the science instruments [M. Kikuchi *et al.*, 2011]. It controls the power of each science instrument, event triggering, data acquisition, data compression, and data processing for the command and telemetry communication. There is another onboard computer, named the Mission

Data Processor (MDP), at the upper level from SHU, which mainly controls the command sequence procedure that automatically issues commands to SHU based on a preprogrammed time series of commands. As shown in Figure 1, JEM-GLIMS has a Global Positioning System (GPS) receiver to obtain the precise coordinated universal time (UTC) when JEM-GLIMS detects an event. The time accuracy of the GPS is in the order of μs .

JEM-GLIMS is installed inside a bus system named the Multi-mission Consolidated Equipment (MCE). As four other mission instruments

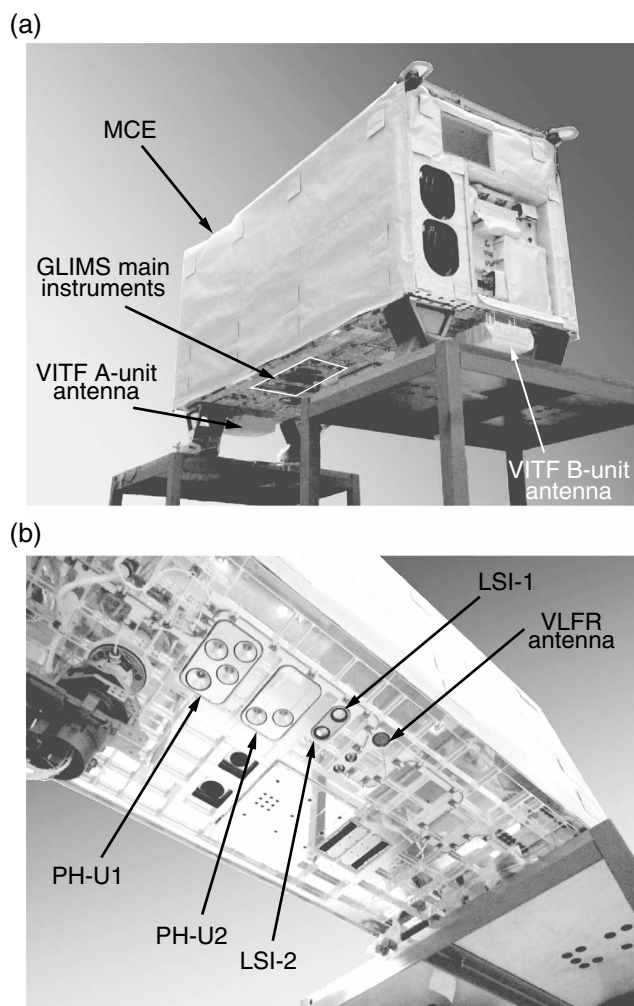


Figure 4. (a) Snapshot of MCE. The JEM-GLIMS main instruments are installed in the base plate of MCE in the nadir direction. The two VITF antennas are installed at both the edges of the MCE base plate. (b) Close-up view of the MCE base plate. From the left to the right side, PH-U1, PH-U2, LSI, and the VLFR antenna are aligned.

other than the JEM-GLIMS instrument are also installed, JEM-GLIMS is one of the science payloads for MCE. Pictures of MCE are presented in Figures 4a and 4b. The dimensions of the MCE are $180 \times 100 \times 80 \text{ cm}^3$. As shown in Figure 4a, the JEM-GLIMS main instruments are located at the bottom center of MCE, and the two VITF antennas are installed at the edges of the MCE base plate. Figure 4b is a close-up view of the base plate of MCE facing toward the Earth's surface. In this picture, the position of LSI optics, PH optics, and the VLFR antenna can be seen.

2.2. Observation Sequence and Trigger Method

The observation geometry of JEM-GLIMS is schematically shown in Figure 5. In this figure, the relation between the square FOV of LSI and the conical FOV of PH are indicated. The ISS orbits at a typical altitude of $\sim 410 \text{ km}$ with a typical velocity of $\sim 8 \text{ km/s}$. As described in section 2.1, the FOVs of LSI and PH are directed toward the nadir direction, but the actual direction slightly changes within a few degrees depending on the ISS attitude.

Figure 6 is a schematic showing the observation sequence of JEM-GLIMS. In this figure, the ISS orbit and Earth are drawn as though looking down from the celestial pole. The JEM-GLIMS observations of lightning and TLEs are conducted when the ISS is in the Earth's shadow and above the nightside. As the orbital period of the ISS is $\sim 90 \text{ min}$, the maximum observation period becomes $\sim 30 \text{ min}$ in one orbit. To avoid possible damage to the high-voltage units used for PH due to the precipitation of high-energy particles, JEM-GLIMS observations are interrupted when the ISS locates over the South Atlantic Anomaly (SAA).

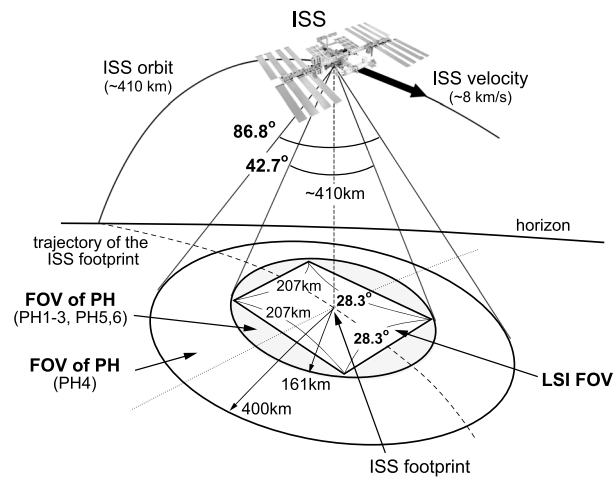


Figure 5. Schematic showing the observation geometry and the FOVs of LSI and PH. The typical orbital altitude and the speed of the ISS are ~410 km and ~8 km/s, respectively. LSI has the square FOV of 28.3° × 28.3°. PH1–3, PH5, and PH6 have a conical FOV of 42.7°, which is nearly equal to the circumscribed circle of the LSI FOV. PH4 has a wider FOV (86.8°) than the other PH channels.

JEM-GLIMS science data are not continuously stored; they are only stored when JEM-GLIMS detects a strong transient optical emission. Output signals from each instrument are temporarily recorded in the ring-buffer memories in SHU, which are shown as “8 MB S-RAM” in Figure 1. When the trigger instrument detects a signal exceeding the trigger threshold level, which can be arbitrarily set by a command, the data buffering is stopped and the data is forwarded from the S-RAM to the 128 MB flash-ROM so that they can be downlinked to the ground system through the ISS system. When the data forwarding is completed, the data buffering will automatically start again to wait the coming trigger signal. The trigger sequence and the data length of each instrument for one trigger event are schematically shown in Figure 7. In usual observations, PH is selected as the trigger instrument. When the output signal of PH exceeds the trigger threshold level, four consecutive LSI image data from one frame before the trigger time are stored. For the PH light curve and VLFR waveform, data for a 512 ms time period from 100 ms before the trigger time are stored. VITF detects VHF pulses on the basis of its own trigger logic, and stores the waveform data on the ring-buffer memory located in the VITF electronics at a rate of 2.56 μs time length per single pulse data. This ring-buffer memory has the capability to hold 130 VHF pulse data. When the trigger signal is exploded from the PH, the data buffering stops when it passes a specific delay time (T_{delay}) after the trigger time, which can be arbitrarily set by a command. Then, a stack of these pulse data are grabbed from the ring-buffer memory into the flash-ROM by SHU and downlinked.

For the PH light curve and VLFR waveform, data for a 512 ms time period from 100 ms before the trigger time are stored. VITF detects VHF pulses on the basis of its own trigger logic, and stores the waveform data on the ring-buffer memory located in the VITF electronics at a rate of 2.56 μs time length per single pulse data. This ring-buffer memory has the capability to hold 130 VHF pulse data. When the trigger signal is exploded from the PH, the data buffering stops when it passes a specific delay time (T_{delay}) after the trigger time, which can be arbitrarily set by a command. Then, a stack of these pulse data are grabbed from the ring-buffer memory into the flash-ROM by SHU and downlinked.

3. Summary of JEM-GLIMS Observations

3.1. Nadir Observations of Lightning Emissions

JEM-GLIMS was launched by the H-IIB rocket on 21 July 2012 from the Tanegashima Space Center and transported to the ISS by the H-II Transfer Vehicle (HTV). HTV docked with the ISS on 27 July 2012, and the MCE was finally installed at JEM EF on 9 August 2012. After the initial checkout operation, JEM-GLIMS started continuous observations on November 2012. To date, all JEM-GLIMS instruments are working normally and continuing the acquisition of high-quality data. Figure 8 shows a gallery of lightning emissions detected

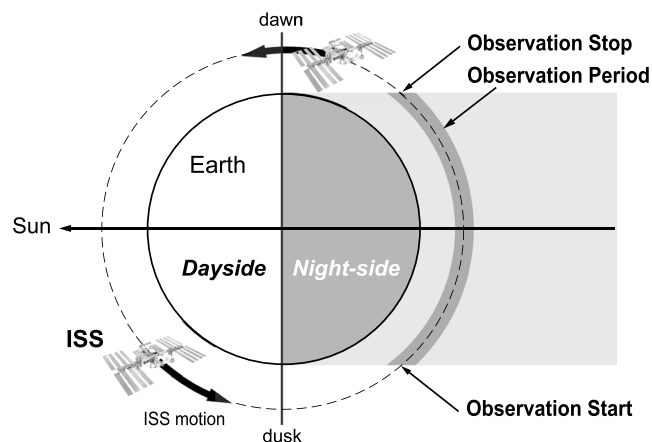


Figure 6. Schematic showing the observation sequence of JEM-GLIMS.

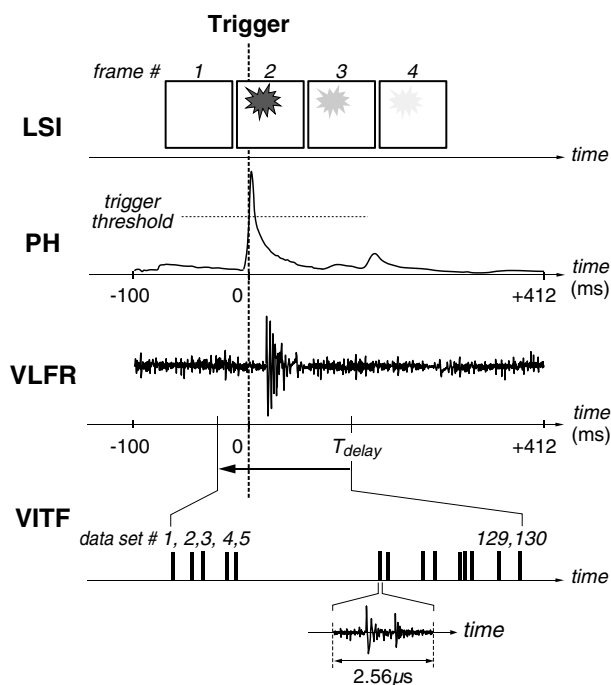


Figure 7. Schematic showing the trigger sequence of JEM-GLIMS. In this trigger routine, PH is selected as the trigger instrument, and the trigger threshold level can be arbitrarily selected by a command. When the trigger signal is exploded from PH, LSI image data are obtained for four consecutive frames from one frame before the trigger time. As for PH and VLFR, light curve and waveform data are recorded from 100 ms before the trigger time to 412 ms after the trigger time. As for VITF, waveform data for 130 VHF pulse events detected before $t = T_{\text{delay}}$ ms are stacked into one data file and stored.

molecules if lightning currents flow at lower altitude in the thunderclouds.

3.2. Global Distribution of JEM-GLIMS Events

The global distribution of lightning events detected by JEM-GLIMS optical instruments for the period between 20 November 2012 and 31 January 2014 is plotted in Figure 9. In this time period, a total of 3131 lightning events were detected by JEM-GLIMS optical instruments. Note that Figure 9 is not a plot of the occurrence rates of lightning events normalized by the unit area and unit observation time (i.e., events/km²/month) but a simple scatterplot of these lightning events. Although the red dots in this figure correspond to the ISS location where JEM-GLIMS detected the lightning events, we think they are almost comparable to the actual lightning distribution on this plotting scale. Note that latitudinal areas over $\pm 51^\circ$ are hatched due to the orbital inclination angle of the ISS. Furthermore, the areas over South America and the southern part of the Atlantic Ocean are also hatched because the ISS locates over SAA where JEM-GLIMS does not carry out observations, as described in section 2.2. It is clear that most of the lightning events were detected over Africa, Southeast Asia, Middle America, and the northern part of South America. Some of the events were detected over the oceanic area, such as over the central Pacific Ocean. All these characteristics are fairly consistent with the global lightning distribution derived from the MicroLab-1/OTD and TRMM/LIS measurements [Boccippio *et al.*, 2000; Christian *et al.*, 2003].

3.3. Seasonal Variations of JEM-GLIMS Lightning Distribution

Figures 10a–10d show the distribution in the northern spring (from March to May), summer (from June to August), fall (from September to November), and winter (from December to February) seasons, respectively. As all lightning events presented in Figure 9 are used for these plots, it should be noted that two seasons of the lightning events in November, December, and January are used. According to Figures 10a and 10c, lightning events in the northern spring and fall seasons are almost symmetrically distributed in the Northern and Southern Hemispheres. In contrast, lightning events in the northern summer and winter seasons shown in

by LSI-1 at different times and dates. In this figure, the intensities of the emission are indicated by the blue-to-white color contour with relative values, and the color scale is given at the bottom of each image. Note that these data are the expanded images trimmed from the original 512×512 size LSI data and that the ground-level horizontal scale is superimposed on each image. It is clear that the horizontal dimension of lightning emissions is approximately 20–30 km, which is typical of the events detected by LSI-1. Moreover, it is found that the shape of the lightning emission is not like a simple Gaussian distribution but a complicated structure, which is determined by the cloud structure and the three-dimensional structure of lightning currents in the thundercloud. In particular, the right-side edge of the lightning emission in Figure 8e seems to be lacking, which is likely obscured by another dense cloud located at a higher altitude than the cloud scattering the lightning emission. On the other hand, the shape of the lightning emission in Figure 8f is quite sharp. This may indicate that lightning currents flow near the top of the thundercloud or that no interfering clouds exist between the sensor and the lightning because the outline of the lightning optical emissions is vague, owing to the multiple scattering effects of the cloud

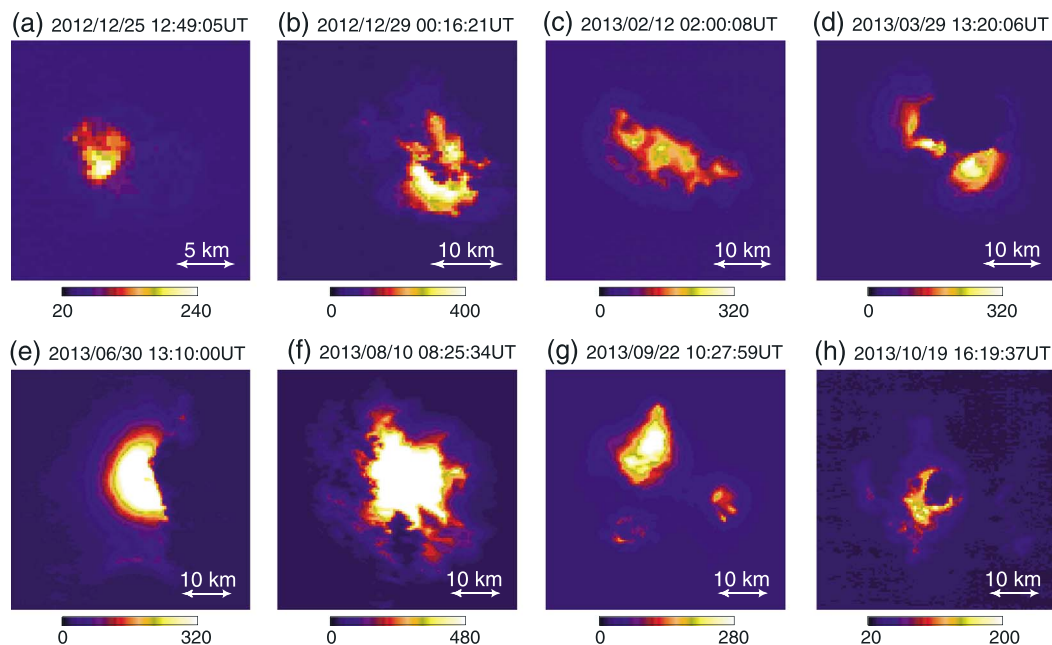


Figure 8. Example of the lightning emissions measured by LSI-1. For each event, single-frame image data where the intensity of the lightning emission reached the maximum is selected. Intensities of the optical emissions are indicated by the color contour, and the relative intensity values are given at the bottom of each image.

Figures 10b and 10d are centered in the Northern and Southern Hemispheres, respectively. These characteristics are particularly noticeable in Africa and Southeast Asia. As lightning activity tends to be enhanced in the local summer hemisphere, JEM-GLIMS succeeds in monitoring such lightning activities as expected. Note that lightning events in winter thunderstorms can be also detected near Japan and the Mediterranean Sea, as shown in Figure 10d. All the seasonal variations shown in Figure 10 are comparable to previous ground-based and satellite lightning observations [Boccippio et al., 2000; Rakov and Uman, 2003; Altaratz et al., 2003; Christian et al., 2003; Price and Federmesser, 2006; Kotroni and Lagouvardos, 2008].

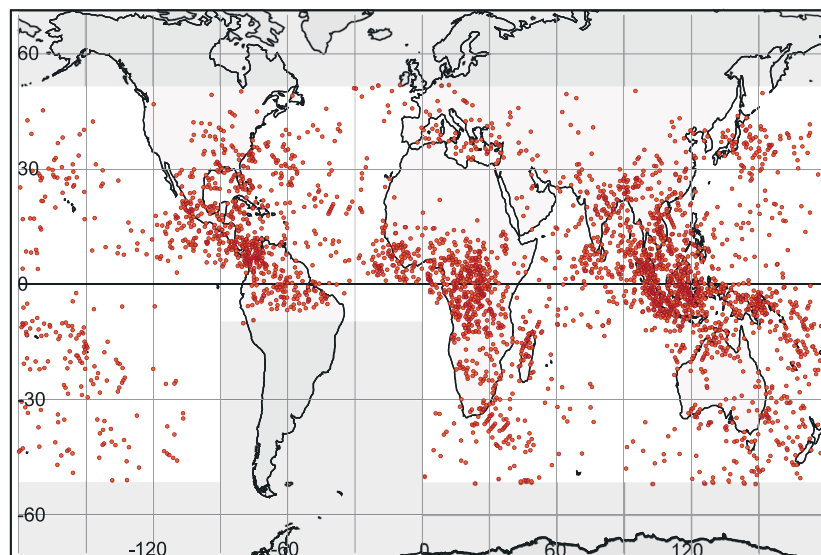


Figure 9. Global map of lightning events detected by JEM-GLIMS optical instruments for the period between 20 November 2012 and 31 January 2014.

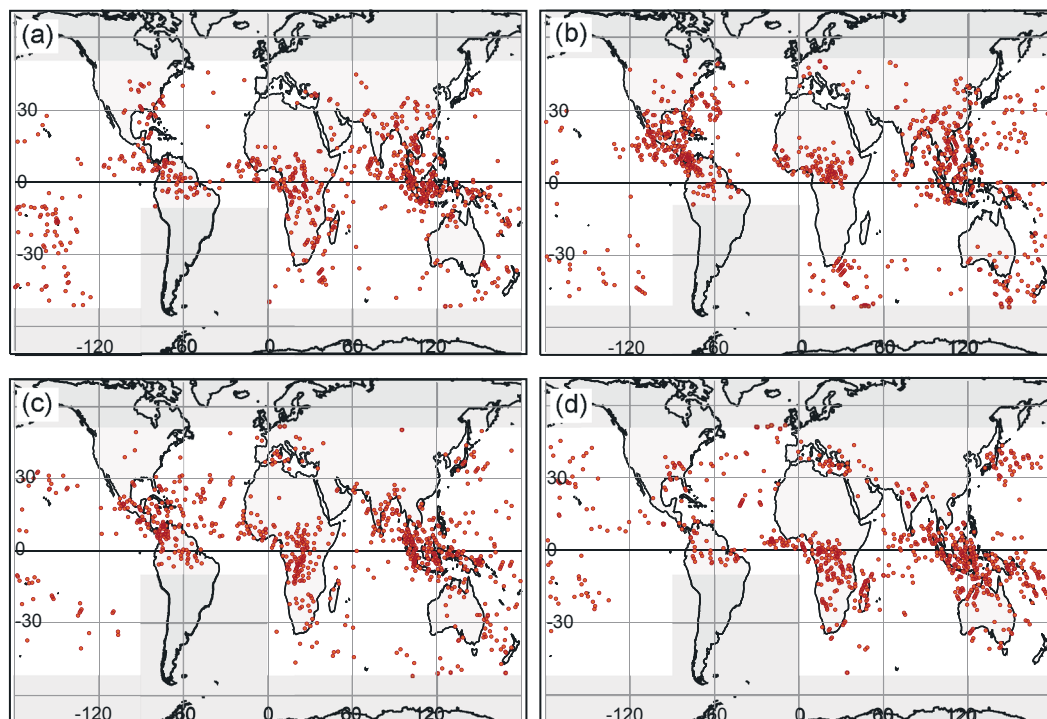


Figure 10. Seasonal variations of lightning events detected by JEM-GLIMS optical instruments. (a) Lightning distribution in the northern spring season (March–May), (b) in the northern summer season (June–August), (c) in the northern fall season (September–November), and (d) in the northern winter season (December–February).

4. Optical Properties of Lightning Events

LSI imaging observations can provide morphological data on the spatiotemporal changes of the lightning emissions occurring in the FOV with a 33 ms time resolution, while the photometric observations of PH can provide precise temporal changes of the absolute intensities of lightning emissions with a 50 μ s time resolution. The major advantages of nadir observations compared with limb observations are that the entire shape and spatial distribution of the lightning emission can be quantitatively measured and that the distance between the lightning location and the instruments and associated atmospheric transmittance does not drastically change. Thus, it is expected that the characterization of the discharge processes and the distinction between CG and IC discharges can be achieved for the first time from these nadir imaging and photometric observations of JEM-GLIMS.

4.1. Cloud-to-Ground Discharge Event

There were many lightning events observed by JEM-GLIMS optical instruments that originated in CG discharges. One example of a CG discharge event is presented in Figure 11. This event was detected at 20:40:35.13523 UT on 30 August 2013, when the ISS was located at 24.481°E, 36.438°S over the Indian Ocean near the southern part of South Africa. The four consecutive images from top to bottom in Figures 11a and 11b are LSI-1 and LSI-2 data, respectively. The second images from the top in these figures are the data obtained at the trigger time. In this event, a strong lightning emission was measured by LSI-1, and the intensity of the emission reached its maximum at one frame after the trigger time (i.e., third frame from the top). As shown in Figure 11b, transient optical emissions are also confirmed in LSI-2 images. Figure 11c shows the light curve data obtained by PH with absolute intensity values. In this plot, the time at $t = 0$ ms is the trigger time at 20:40:35.13523 UT when the output signal of PH exceeded the trigger threshold level. Figure 11d shows the magnetic field waveform data in the ELF frequency range measured at Syowa station (39.506°E, 69.018°S), Antarctica. The solid and dashed lines correspond to the waveforms in the magnetic north-south and east-west components, respectively. The time period corresponding to the PH light curve data and the trigger time are indicated in this figure. From this ELF data, it is identified that a transient Schumann resonance (SR) waveform with an amplitude of ~ 15 pT was detected at 20:40:35.148 UT in both components. Taking into account the optical propagation time of 1.40 ms from the thundercloud to the ISS, assuming that the light

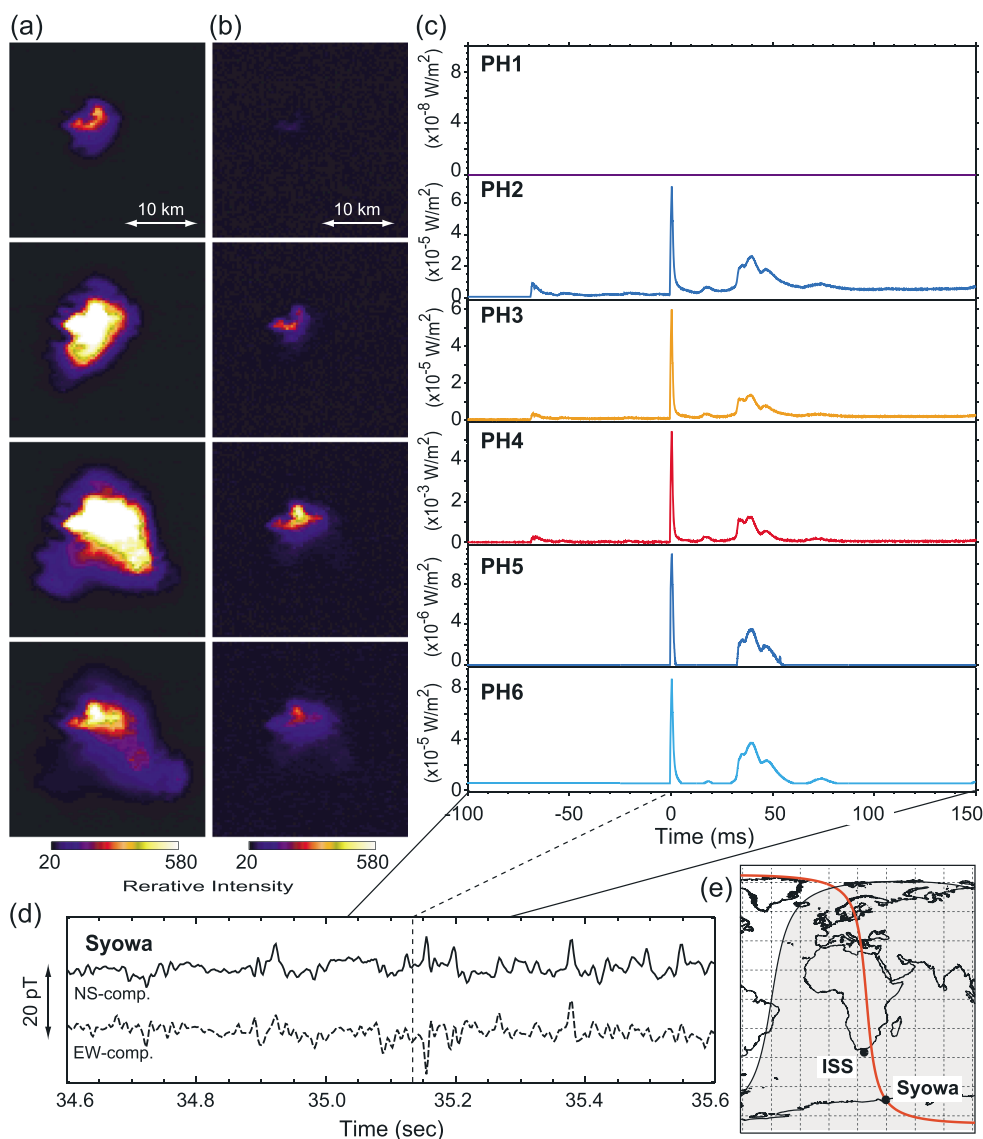


Figure 11. CG discharge event detected by JEM-GLIMS optical instruments at 20:40:35.13523 UT on 30 August 2013. (a and b) Four consecutive image data obtained by LSI-1 and LSI-2, respectively. The second images from the top correspond to the frame obtained at the trigger time. Intensities of the emission are expressed by the color contour, and the relative intensities are given at the bottom of the image. (c) Light curve data obtained by the six PH channels. Absolute intensities (W/m^2) of each channel are indicated. In this plot, $t = 0$ ms corresponds to the trigger time (20:40:35.13523 UT). (d) Plot of the ELF magnetic field waveform data measured at Syowa station, Antarctica in the time period 20:40:34.6–35.6 UT. Solid and dashed lines are the waveform data in the north–south and east–west component, respectively. (e) Propagation path of the transient SR wave detected at 20:40:35.148 UT (red line). The locations of the ISS footprint and Syowa station are indicated using the solid circles. The dark area corresponds to the nightside.

source in the thundercloud was located at 10 km altitude, the distance of $\Delta\theta = 3.74$ Mm between the ISS footprint and Syowa station, and the wave propagation time of $\Delta t = 15.57$ ms from the ISS footprint to Syowa station assuming a propagation velocity of $v = 0.8c$ suggested by Füllekrug and Constable [2000] and Sato and Fukunishi [2003], the expected time of the wave arrival at Syowa station becomes 20:40:35.149 UT. This estimated time is comparable to the time when the transient SR wave was actually detected at Syowa station. The red solid line in Figure 11e shows the propagation path of the transient SR wave detected at 20:40:35.148 UT. The solid circles and dark-colored hatched area in this figure are the locations of the ISS footprint and Syowa station and nightside, respectively. Using the analysis technique of Sato and Fukunishi [2003] and Sato et al. [2008], the propagation path of the transient SR wave was estimated from the ELF waveform data shown in Figure 11d. As shown in this figure, the direction of the ISS footprint from the Syowa station is very close to

that of the propagation path. The bearing angle of the ISS footprint from the Syowa station is -22.13° (westward from the north), whereas the bearing angle of the propagation path of the transient SR wave is -14.39° . Thus, we concluded that the transient SR wave detected at 20:40:35.148 UT at Syowa station was actually excited by the CG discharge observed using the JEM-GLIMS optical instruments. Based on the polarity of the transient SR wave, the parent lightning discharges of this optical event were identified as a +CG discharge.

As shown in Figure 11c, continuous weak emissions were measured in the time period from $t = -70$ ms to $t = 0$ ms. It can be deduced that these emissions originated in the discharge processes inside the thundercloud, that is, preliminary breakdown (PB) [Nag and Rakov, 2008; Baharudin et al., 2012]. In this time period, the tips of the stepped leader seemed to develop in the thundercloud and made a touchdown to the ground. Then, the strong impulsive emission at $t = 0$ ms is likely to be emitted by the return stroke. Finally, the gradual enhancement at the time period of $t = 30$ – 80 ms may be associated with in-cloud discharges when the positive charges in the thundercloud are continuously neutralized.

All PH channels except for PH1 succeeded in detecting the optical emissions of the +CG discharge. The reason for no signal in PH1 light curve data must be caused by the severe (or almost perfect) absorption of FUV emissions in the atmosphere, even if the lightning had the capability to excite N_2 LBH emissions. Therefore, no signal in PH1 data implies the absence of TLEs. Thus, we think that the optical emissions measured by LSI-2 in Figure 11b originated in the lightning emissions that overcame the atmospheric absorption and succeeded in reaching the ISS altitude. At the PB stage, no effective signal was detected in PH5 and PH6. PB emissions in the wavelength range of 310–321 nm must be too weak to be detected by PH5 due to severe atmospheric absorption. The reason for no signal in PH6 may come from no emission of $N_2^+ 1N(0,0)$ at 391.4 nm or only weak continuum emissions in the wavelength range of 386–397 nm. For each PH channel, the absolute intensity ratio of the return stroke optical emission at $t = 0$ ms to the in-cloud discharge optical emission at $t = 30$ – 80 ms seem to be different from each other. This may be affected by differences in the altitude where the discharge currents flowed.

For the gradual increase in optical emissions during the time period of $t = 30$ – 80 ms, the emissions can be possibly considered as another subsequent return stroke and not as in-cloud discharges. Indeed, a faint transient SR waveform can be confirmed at approximately 20:40:35.2 UT after the CG-related transient SR wave at 20:40:35.148 UT as shown in Figure 11d. However, precisely determining the discharge processes only from the JEM-GLIMS and ground-based ELF observation data is difficult. To achieve this, we intend to further compare the JEM-GLIMS optical data with the ground-based ELF/VLF/low-frequency (LF)/VHF measurement data.

4.2. Intracloud Discharge Event

One example of an IC discharge event is presented in Figure 12. The format of this plot is the same as Figure 11. This event was observed at 14:19:48.69132 UT on 19 June 2013, when the ISS was located at 178.810°W , 30.588°S over the Pacific Ocean. As shown in Figures 12a and 12b, both LSI-1 and LSI-2 detected intense lightning emissions in the third frame. Figure 12c is a plot of the light curve data obtained by PH. In this event the intermittent multiple optical pulses were measured by PH2–6 for the time period from $t = -6$ ms to $t = 5$ ms. Figure 12d is a plot of ELF magnetic field waveform data acquired at Syowa station in the time period 14:19:48.4–49.4 UT. Considering the optical propagation time of 1.40 ms from the assumed light source at the altitude of 10 km to the ISS altitude of 430 km, the distance of $\Delta\theta = 8.51$ Mm between the ISS footprint and Syowa station, and the wave propagation time of $\Delta t = 35.45$ ms from the ISS footprint to Syowa station with an assumed propagation velocity of $v = 0.8c$, the expected time of the wave arrival at Syowa station would be 14:19:48.725 UT. As seen in Figure 12d, there is no clear transient SR waveform at around the PH trigger time. Thus, we concluded that this optical signal originated in an IC discharge.

The multiple optical pulses shown in Figure 12c well resemble the time variation of the electric field in the radio frequency band [Rakov and Uman, 2003; Sharma et al., 2005]. It is deduced that this type of the multiple optical emission occurring within a few milliseconds may be typical of IC discharges. From a calculation of the intensity ratio between different PH channels, it would be possible to identify the relative differences of the height where lightning discharges occur, which would lead to a better distinction of IC and CG discharges as proposed by Adachi et al. [2012]. Initial results showing the relative differences of the lightning altitudes derived from JEM-GLIMS optical data will be presented in other papers.

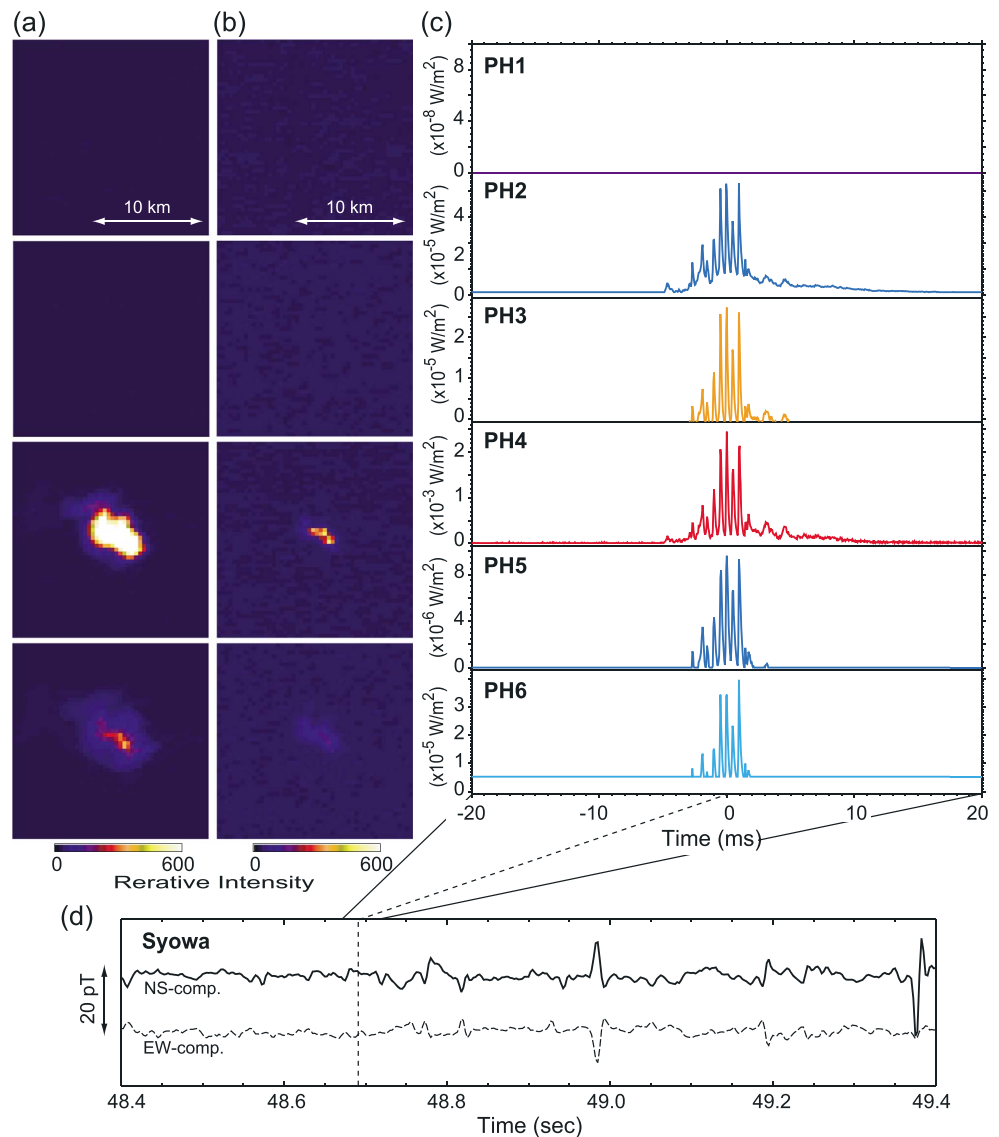


Figure 12. IC discharge event detected by the JEM-GLIMS optical instruments at 14:19:48.69132 UT on 19 June 2013. (a and b) Image data obtained by LSI-1 and LSI-2, respectively. (c) Light curve data obtained by the six PH channels. (d) Plot of the ELF magnetic field waveform data measured at Syowa station in the time period 14:19:48.4–49.4 UT. Solid and dashed lines are the waveform data in the north-south and east-west component, respectively.

5. Lightning Events With FUV Emissions

5.1. TLE Emissions

The existence of FUV emissions from TLEs has been confirmed by the number of previous studies. FUV emissions of sprites and elves have been identified by the observations of ISUAL on board the FORMOSAT-2 satellite from space [Kuo *et al.*, 2005a, 2007; Chang *et al.*, 2010]. Using a simulation technique, optical emissions from sprite halos were estimated, and it was predicted that FUV emissions should be high enough to be detected from the ISS altitude [Gordillo-Vázquez *et al.*, 2011]. The detection of FUV emissions, which can be achieved by PH1, strongly suggests the occurrence of TLEs.

An example of an optical event accompanying FUV emissions is presented in Figure 13. The format of this figure is identical to that of Figure 11. This event was detected at 05:59:09.97813 UT on 11 August 2013, when ISS was located at 69.047°W, 36.025°N over the Atlantic Ocean near the northeast of North America. Figures 13a and 13b are LSI-1 and LSI-2 image data expanded from the original 512 × 512 size image data, respectively. According to the original LSI image data, it is found that this optical emission occurred near the

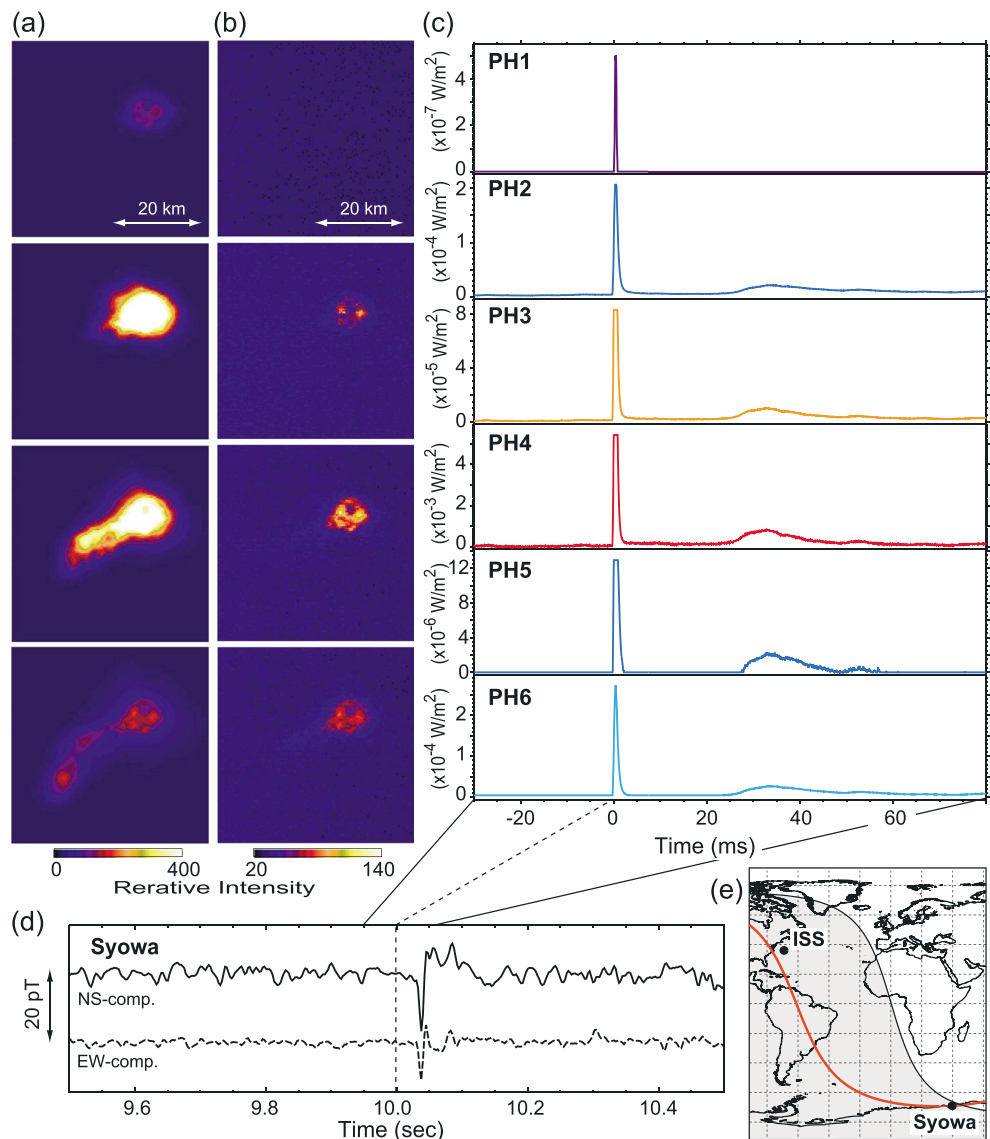


Figure 13. TLE detected by the JEM-GLIMS optical instruments at 05:59:09.97813 UT on 11 August 2013. (a and b) Image data obtained by LSI-1 and LSI-2, respectively. (c) Light curve data obtained by the six PH channels. (d) Plot of the Syowa ELF magnetic field waveform data in the time period 05:59:09.5–10.5 UT. Solid and dashed lines are the waveform data in the north-south and east-west component, respectively. (e) Propagation path of the transient SR wave detected at 05:59:10.035 UT (red line). The locations of the ISS footprint and Syowa station are indicated using the solid circles. The dark area corresponds to the nightside.

nadir point. As measured by LSI-1 in Figure 13a, the lightning optical emission first appeared near the right top corner at the first frame, then the intensity of the emission suddenly increased at the second frame, and finally the bright area of the emission rapidly expanded toward the left bottom corner at the third and fourth frames with a velocity of ~ 440 km/s. In Figure 13b, a weak but structured emission was detected by LSI-2, but the position of the optical emission did not change and remained almost the same. Figure 13c shows the light curve data of the six PH channels. It is clear that the impulsive FUV emission was detected by PH1 at $t = 0$ ms in this event. As the PH1 light curve was unfortunately saturated, the peak intensity was estimated to be $> 5.0 \times 10^{-7}$ W/m². In the other PH channels, the strong impulsive optical emission and the following gradual optical enhancement were observed at $t = 0$ ms and $t > 25$ ms, which must be related to the return stroke and subsequent in-cloud discharges (or another subsequent return stroke), respectively. As these optical characteristics are quite similar to those shown in Figure 11, this event seems to be a CG discharge event. Figure 13d is a waveform plot of ELF magnetic field perturbations measured at Syowa station

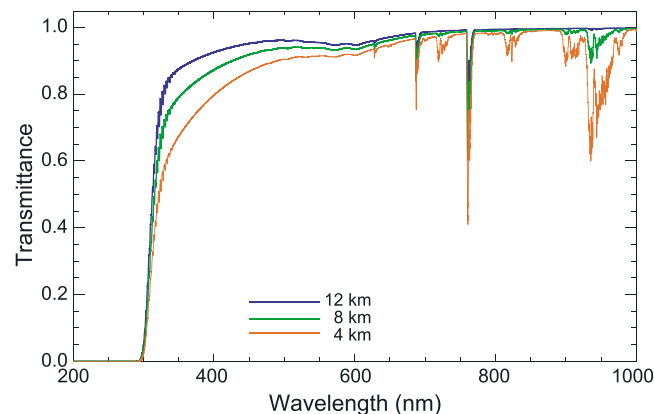


Figure 14. Modeled atmospheric transmittance in the wavelength range of 200–1000 nm calculated by MODTRAN. Each line shows the transmittance from a light source located at the 4, 8, and 12 km altitude in the zenith.

during 05:59:09.5–10.5 UT. At 05:59:10.035 UT, a transient SR wave with an amplitude of ~ 20 pT was detected, which must be related to the impulsive emission at $t = 0$ ms in Figure 13c. As the distance between Syowa station and the ISS footprint is $\Delta\theta = 14.45$ Mm and the propagation time of the ELF wave from the ISS footprint to Syowa station is $\Delta t = 60.20$ ms, the expected detection time of the ELF wave is mathematically calculated to be 05:59:10.037 UT. Figure 13e shows the propagation path of the transient SR wave detected at 05:59:10.035 UT at Syowa station. The bearing angle of the ISS footprint from the Syowa station and the bearing angle of the propagation path are -92.22° (westward from the north) and -99.97° , respectively. Because the transient SR wave propagated from the source to the observer in the nightside, these two bearing angles are probably comparable. Thus, the transient SR wave is confirmed to be excited by the lightning discharge measured by JEM-GLIMS. From the polarization of the transient SR wave this lightning event was a +CG discharge.

Lightning discharge may excite N_2 LBH emissions by itself, but this has never been confirmed by ground-based observations. However, such FUV emissions are perfectly absorbed by the atmosphere and do not reach the ISS altitude. Figure 14 shows the modeled atmospheric transmittance from light sources located at different altitudes to the zenith in the wavelength range of 200–1000 nm calculated by the Moderate Resolution Atmospheric Transmission (MODTRAN) code. In this calculation, the altitudes of the light sources are assumed to be 4, 8, and 12 km and are indicated by the red-, green-, and blue-colored solid lines in Figure 14, respectively. The atmospheric transmittance below 300 nm is $\sim 0\%$. Although the atmospheric transmittance below 200 nm cannot be calculated by the MODTRAN code, it is thought that atmospheric ozone and oxygen molecules still have enough capability to absorb FUV emissions. So the presence of FUV emissions in the PH1 channel strongly supports the evidence for a TLE occurrence.

As seen in Figure 13b, the transient optical emissions occurred over the area of strong lightning emissions shown in Figure 13a. To distinguish the occurrence type of TLEs in this event, to clarify the spatial distribution of TLEs, and to identify the relation to the parent CG discharges, further detailed analyses are needed. In fact, we have already developed the data processing techniques to do so, according to (1) a subtraction of the appropriately scaled LSI-1 image from LSI-2 image, (2) a calculation of the intensity ratio between different PH channels, and (3) an estimation of the polarization and CMC for the parent CG discharges of the event using ground-based ELF measurement data. For procedure (1), the scaling factor can be statistically determined by calculating the intensity differences between the LSI-1 and LSI-2 image data for events containing only lightning optical emissions. By multiplying the scaling factor and LSI-1 image data and by subtracting the scaled LSI-1 image data from the LSI-2 image data, we can selectively extract only the TLE emissions [Sato *et al.*, 2013]. From a synthetic comparison of these results, it is possible to distinguish the types of TLEs. The detailed introductions of these procedures and results are beyond the scope of this paper and will be summarized in other papers soon in due course.

5.2. Elves Event

One more example of an optical event accompanying FUV emissions is presented in Figure 15. The format of this figure is same as that of Figure 11. This event occurred at 16:26:33.80681 UT on 15 October 2013, when

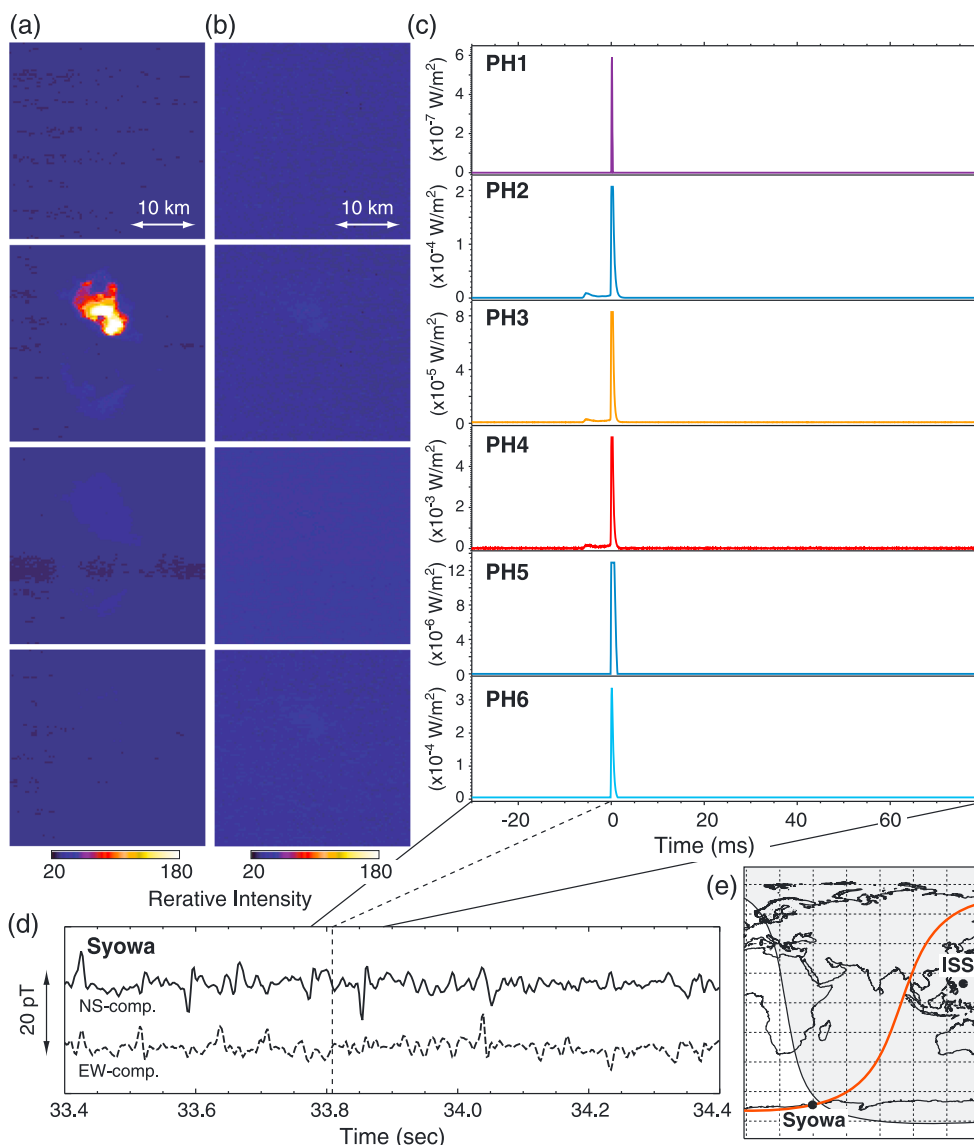


Figure 15. Elves event detected by the JEM-GLIMS optical instruments at 16:26:33.80681 UT on 15 October 2013. (a and b) Image data obtained by LSI-1 and LSI-2, respectively. (c) Light curve data obtained by the six PH channels. (d) Plot of the Syowa ELF magnetic field waveform data in the time period 16:26:33.4–34.4 UT. Solid and dashed lines are the waveform data in the north-south and east-west component, respectively. (e) Propagation path of the transient SR wave detected at 16:26:33.853 UT (red line). The locations of the ISS footprint and Syowa station are indicated using the solid circles. The dark area corresponds to the nightside.

the ISS located at 129.829°E, 12.955°N over the Philippine Sea. The optical emission of this event occurred near the nadir position of the ISS.

As shown in Figures 15a and 15b, transient optical emissions from the lightning discharges were detected only by LSI-1 at the trigger time, that is, the second image from the top in Figure 15a. As no optical emission was detected by LSI-2, it is possible to deduce that the possibility of sprite occurrence was quite low in this lightning event. On the other hand, PH light curve data presented in Figure 15c show strong transient optical emissions at $t = 0$ ms, and their peak amplitudes are comparable to those shown in Figure 13c, where strong optical emissions were, however, detected by both LSI-1 and LSI-2. In addition, an intense FUV emission was detected by PH1 in this event at $t = 0$ ms. This strongly implies the occurrence of a TLE.

Figure 15d shows a plot of the ELF magnetic field waveform data acquired at Syowa station in the time period of 16:26:33.4–34.4 UT. In this plot, a transient SR wave with an amplitude of ~ 15 pT was detected at

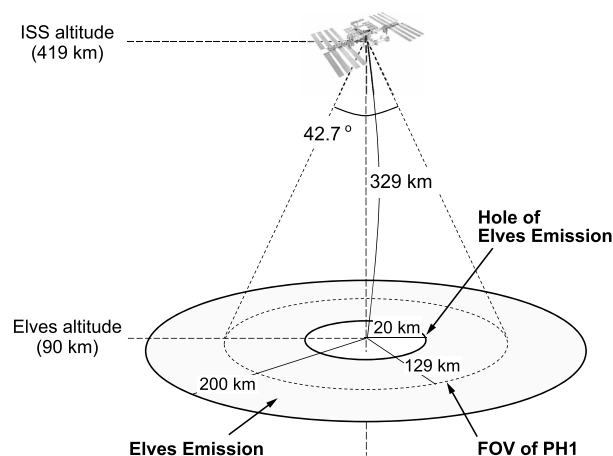


Figure 16. Observation geometry of JEM-GLIMS and the assumed emission area of elves for the event presented in Figure 15.

16:26:33.853 UT mainly in the magnetic north-south component. The propagation time of the optical emission from the light source assumed to be at 10 km altitude to the ISS altitude is 1.36 ms, and the distance from the ISS footprint to Syowa station and the propagation time of the electromagnetic wave for its distance are calculated to be $\Delta\theta = 11.36$ Mm and $\Delta t = 47.33$ ms, respectively. Then, theoretically, the detection time of the transient SR wave at Syowa station, which is assumed to be excited by the lightning discharge observed by LSI-1, becomes 16:26:33.85278 UT. This estimated detection time is consistent with the time when the transient SR wave was actually measured. The red solid line in Figure 15e is the propagation path of the transient SR wave detected at 16:26:33.853 UT at Syowa station. The solid circles and dark-colored hatched area in this figure are the locations of the ISS footprint and Syowa station and nightside, respectively. Note that the Syowa station was located in the dayside, whereas the lightning event detected by the JEM-GLIMS optical instruments occurred in the nightside. As shown in this figure, the propagation path crosses a point rather far from the ISS footprint. The bearing angle of the ISS footprint from the Syowa station and the bearing angle of the propagation path are calculated at $+85.59^\circ$ (eastward from the north) and $+54.96^\circ$, respectively. The difference between these angles is somewhat larger than that in Figures 11e and 13e. This may be caused by the so-called “day/night terminator effect” on the propagating SR waves [Nickolaenko and Hayakawa, 2002]. When SR waves propagate across the terminator line, the day/night asymmetry of the wave reflection height profoundly modifies the amplitudes of the SR waves. Thus, the estimation error of the wave propagation direction increases because the bearing angle is calculated from the polarization axis of the transient SR waves in a Lissajous plot of the horizontal magnetic field data [Sato and Fukunishi, 2003; Sato et al., 2008]. Therefore, we concluded that the transient SR wave at 16:26:33.853 UT was generated by the lightning discharge in Figure 15a. From the polarity of the transient SR wave, this lightning event was identified as a $-CG$ discharge. Considering all of the above facts, this event was identified as an elves event.

So far, many elves events have been detected by ISUAL on board the FORMOSAT-2 satellite [Kuo et al., 2005b, 2007; Chang et al., 2010]. Chang et al. [2010] reported that the intensity of the FUV emission for the dimmest elves is $< 1 \times 10^4$ photons/cm². Consequently, the photon number measured at the ISS altitude (I_{ISUAL}) becomes $< 8 \times 10^{12}$ photons/m²/s under the following four assumptions: (1) the time constant of elves is 1 ms, (2) the distance between ISUAL and elves is 2700 km, (3) the distance between JEM-GLIMS and elves is 300 km, and (4) the atmospheric transmittance does not change for this conversion. Note that the impulsive signal of PH1 at $t = 0$ ms, shown in Figure 15c, is not saturated. The peak intensity of the impulsive PH1 signal is estimated to be 5.90×10^{-7} W/m². Here the following two assumptions are used to calculate the photon from the peak intensity: (1) the FUV spectrum of elves is the same as that of the sprite halo provided in Figure 5 of Gordillo-Vázquez et al. [2011] and (2) the optical emission lines at 178, 184, 193, 203, and 212 nm only contribute to the spectral intensity in the PH1 band width. Then, the photon number (I_{GLIMS}) is calculated to be 5.62×10^{11} photons/m²/s. From the photon numbers derived from the ISUAL and JEM-GLIMS measurements, $I_{\text{GLIMS}}/I_{\text{ISUAL}}$ is 0.07. This ratio is quantitatively evaluated because the observational geometry of JEM-GLIMS and the relative portion of the elves emission are known or can be postulated. Figure 16 shows the observation geometry of JEM-GLIMS and an assumed emission area of elves. In this event, the ISS was located at 419 km altitude, and the parent lightning discharges of elves occurred near the nadir point. Therefore, we assumed that elves occurred just beneath the ISS at 90 km altitude. The radius of the elves emission and the radius of the central hole in the elves emission are assumed to be 200 km and 20 km, respectively [Nagano et al., 2003; Marshall et al., 2010]. As PH1 has a conical FOV of 42.7° , the radius of the observational area of PH1 at 90 km becomes 129 km. Assuming that the optical emission of elves is spatially homogeneous, the intensities detected by the JEM-GLIMS and ISUAL optical instruments are solely proportional to the area of the elves emission within the PH1 FOV. The calculated area of the elves emission within the PH1 FOV (S_{GLIMS}) is

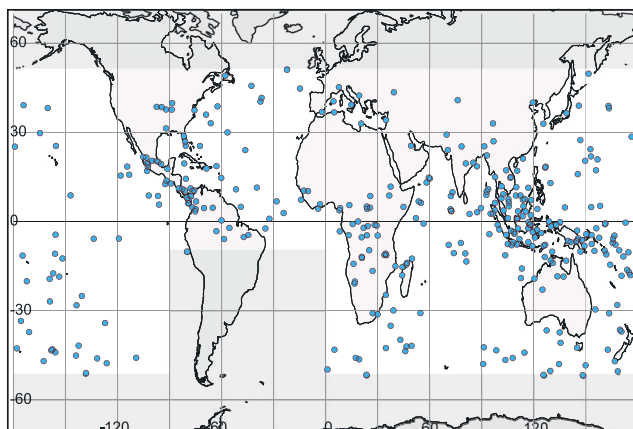


Figure 17. Global map of the lightning events accompanying FUV emissions for the period between 20 November 2012 and 31 January 2014.

$5.1 \times 10^4 \text{ km}^2$. As the ISUAL optical instruments can measure the entire shape of the elves emission, the area (S_{ISUAL}) becomes $1.2 \times 10^5 \text{ km}^2$. Then, $S_{\text{GLIMS}}/S_{\text{ISUAL}}$ is estimated at 0.43, which is approximately 6 times the actual intensity $I_{\text{GLIMS}}/I_{\text{ISUAL}}$ of 0.07. If the photon number I_{GLIMS} is solely determined by $S_{\text{GLIMS}}/S_{\text{ISUAL}}$ and I_{ISUAL} , the value of I_{GLIMS} is expected to be $1.3 \times 10^{12} \text{ photons/m}^2/\text{s}$. This difference may be caused by the difference in the observational geometry between JEM-GLIMS and ISUAL and in the distance from the observer to the elves emission. As ISUAL observes both lightning and TLEs from a few thousand kilometers away in the limb direction, it can observe the entire picture of elves. However, the detectability of the dim elves emission, which is determined by the signal-to-noise ratio of the photometer, weakens. On the other hand, the FOV of PH1 is circular with a radius of 129 km at 90 km. Then, PH1 may only observe a limited portion of the elves emission; however, the detectability of the dim elves emission becomes relatively higher than the ISUAL case.

The instantaneous FOV (iFOV) of LSI is $0.055^\circ \times 0.055^\circ$, which corresponds to $315 \text{ m} \times 315 \text{ m}$ at 90 km. As reported by Nagano *et al.* [2003] and Marshall *et al.* [2010], elves occurs at $\sim 90 \text{ km}$ and has a thin structure in the vertical direction resulting in a thin optical depth for nadir observations from the ISS. As the time constant of elves is typically $< 1 \text{ ms}$ [Nagano *et al.*, 2003], the duration of the emission in the iFOV area must be $< 1 \text{ ms}$ and is much shorter than the LSI exposure time of 33.3 ms. Combining all these data, the lack of elves emission in LSI-1 and LSI-2 images in Figures 15a and 15b must be due to the low sensitivity of LSI to detect the elves emission, which helps elude the detection of elves by LSI.

5.3. Global Map of Lightning Events With FUV Emissions

Figure 17 shows the global distribution of lightning events accompanying the FUV signal detected by JEM-GLIMS for the period between 20 November 2012 and 31 January 2014. The plotting format of this figure is same as that of Figure 9. In this period, a total of 365 events were detected. It is noticeable that the detected FUV events are distributed not only over continental regions but also over oceanic regions equally and that the clear bias seen in Figure 9 does not seem to exist. Based on the TLE measurements by ISUAL, the occurrence rate of sprites over continental regions is higher than that over oceanic regions, while the occurrence rate of elves over oceanic regions is dominant compared with the occurrence rate of the other types of TLEs [Chen *et al.*, 2008]. Hence, it can be assumed that the FUV events detected over continental regions may be associated with sprites and that FUV events over oceanic regions may be related to elves. Using the TLE identification technique from the JEM-GLIMS optical data summarized in the last paragraph in section 5.1, more clear distributions of sprites, elves, and other types of TLEs will be estimated.

6. Electromagnetic Waves Measured by Wave Receivers

6.1. Lightning Whistlers

Lightning discharges can excite intense electromagnetic waves in the broad frequency range. In general, lightning-generated waves have a strong energy in the VLF range, which are reflected at the ground and lower ionospheric boundary and propagate in the Earth-ionosphere waveguide. However, some of the wave energy in the VLF range penetrates into the ionosphere and further into the magnetosphere and forms the well-known lightning whistlers [Helliwell, 1965]. During the 1.5 years operation period of JEM-GLIMS, VLF

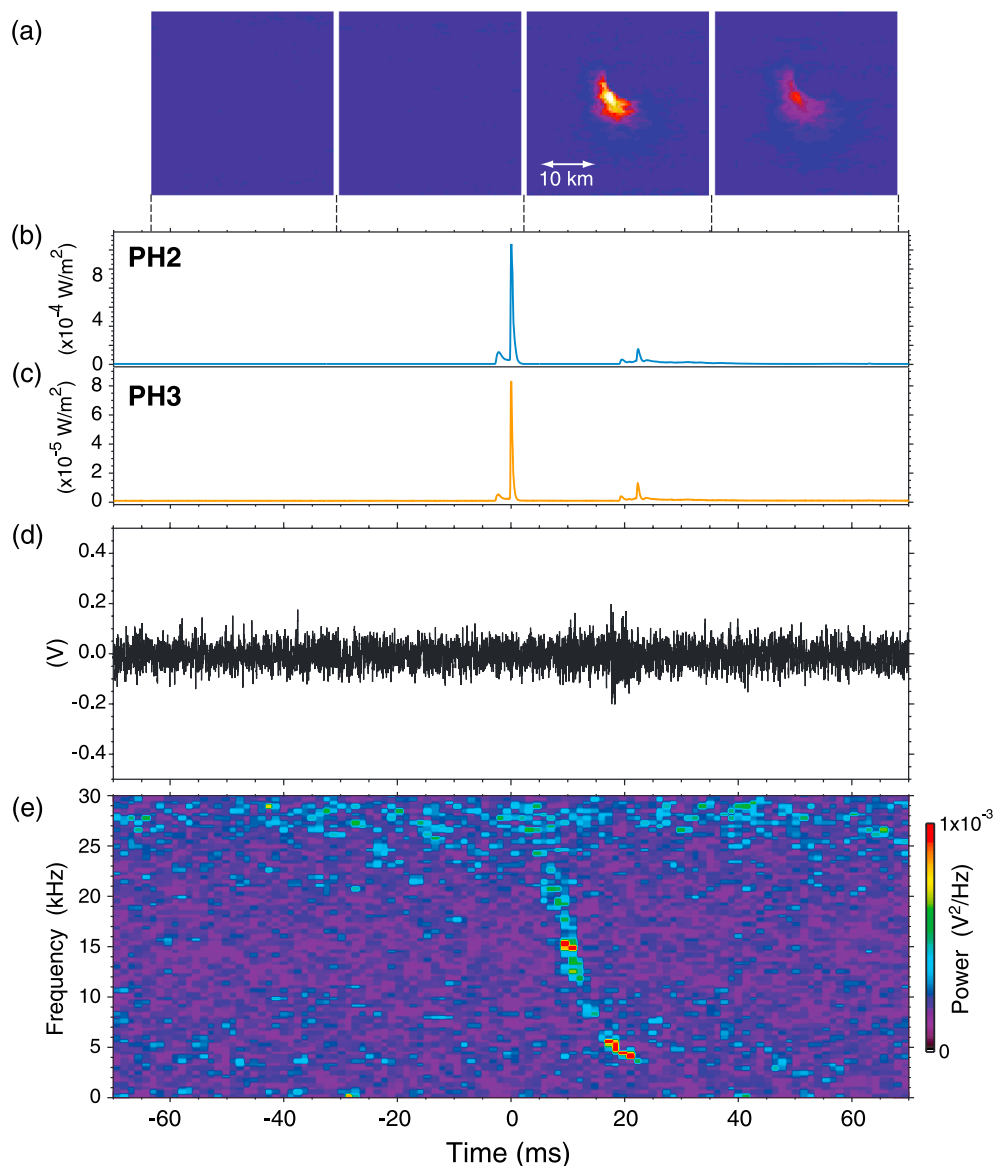


Figure 18. Example of the whistler event detected at 14:21:13.86983 UT on 23 April 2014. (a) Four consecutive LSI-1 image data. (b and c) Light curve data of PH2 and PH3 for the time period from $t = -70$ to 70 ms, respectively. (d) Plot of the electric field waveform data recorded by VLFR from $t = -70$ to 70 ms. (e) Dynamic spectrum of the VLFR waveform data shown in Figure 18d.

successfully detected lightning whistlers that do not cross the magnetic equatorial plane. These whistlers are the so-called fractional hop (0+) whistlers [Smith and Angerami, 1968]. Figure 18 shows an example of a lightning whistler detected by VLFR. This event was triggered by PH at 14:21:13.86983 UT on 23 April 2014. At this time, the ISS was located at 161.734°E , 38.397°S , which is almost the middle point between the east coast of Australia and New Zealand, over the Pacific Ocean.

Figure 18a shows the four consecutive LSI-1 image data, which are expanded images trimmed from the original 512×512 size LSI data, and the dimensions of the images correspond to $32.9 \text{ km} \times 32.9 \text{ km}$ at 10 km altitude. The second image from the left shows the data obtained at the PH trigger time. Figures 18b and 18c are plots of light curve data obtained by PH2 and PH3 for the time period from $t = -70$ ms to $t = 70$ ms, respectively. Although only two light curve plots are presented in this figure, all PH channels except for PH1 detected the transient lightning emission, which had a similar light curve variation to Figures 18b and 18c. The light curve data show a clear impulsive optical emission at $t = 0$ ms. By comparing the light curve data with that of the events in Figures 11, 13, and 15, it is likely that the impulsive optical emission was emitted by the return

stroke of a CG discharge. In Figure 18a, such impulsive optical emission detected by PH at $t = 0$ ms was actually captured at the third image from the left owing to the progressive line-scanning readout characteristics of the CMOS sensor. From the image data, the horizontal dimension of the optical emission is approximately 10 km. Note that the optical emission occurred approximately 64.6 km away from the ISS footprint, assuming that the optical emission was located at 10 km altitude.

Figure 18d is a waveform plot of VLFR electric field data in the time period from $t = -70$ ms to $t = 70$ ms. Note that the amplitude of the waveform is given in relative units. The impulsive onset and following damping oscillations are identifiable at $t = 17$ – 24 ms in this time series. However, the amplitude of this waveform is not larger than that of the background noise waveforms. Thus, the actual onset time of the waveform is not clear only from this waveform plot. Figure 18e shows the dynamic spectrum of the waveform in Figure 18d, which was calculated by the fast Fourier transform (FFT) with a time window of 256 data points (2.56 ms). As the cutoff frequency of the low-pass filter in VLFR electronics is 30 kHz, the spectral amplitude in the frequency range 25–30 kHz gradually increased in this dynamic spectrum. For the $t = 7$ – 24 ms time period, a falling-tone spectral structure appearing from $f = 23$ kHz to $f = 3$ kHz can be confirmed, which is not clearly seen in Figure 18d. This is a very typical spectral characteristic of fractional hop whistlers. Considering the FFT time window of 2.56 ms, the onset time of the whistler is estimated at $t = 9.6$ ms, which corresponds to the time delay from the impulsive PH signal.

A 9.6 ms time delay of the whistler reception from the lightning optical emission (PH) is explained by a group delay in the anisotropic plasma. We calculated the group velocities (V_g) of the plasma waves in the VLF range in the ionosphere and roughly estimated the propagation time from the lightning altitude to the ISS altitude on the basis of the low-frequency approximation [Maeda and Kimura, 1984]. In this calculation, the average electron number densities in the altitude ranges 80–140 km and 140–420 km at this event time and at the ISS location are derived from the International Reference Ionosphere model and are $N_e = 1.3 \times 10^9$ and $1.9 \times 10^{11}/\text{m}^3$, respectively. In this case, the estimated group velocities are $V_g = 2.9 \times 10^8$ m/s in the altitude range 80–140 km and $V_g = 2.4 \times 10^7$ m/s in the altitude range 140–420 km at 23 kHz. Considering the ISS altitude and the horizontal displacement of the lightning emission from the ISS footprint at this event, the time delay of the whistler from the occurrence time of the lightning discharge and the propagation time of the lightning optical emission are 13 ms and 1.4 ms, respectively. Then, the theoretical time delay of the whistler wave from the PH signal becomes 11 ms. It is possible to say that the observed time delay of 9.6 ms is comparable to the estimated time delay, and it is likely that the whistler measured by VLFR originated from the lightning discharge identified by PH.

Note that lightning whistlers are not always measured by VLFR in all lightning events detected by LSI or PH. The number of events where lightning whistlers are not measured but the optical emissions of lightning discharges are measured is much higher than that where both optical emissions and lightning whistlers are measured. For the period between 20 November 2012 and 31 January 2014, 3131 lightning events were detected with the JEM-GLIMS optical instruments, whereas only 157 lightning events were accompanied by lightning whistlers. Thus, the detection rate of lightning whistlers with the JEM-GLIMS VLFR is no more than 5.0%. One reason for this may be due to the length of the VLFR antenna. As the length of the antenna is rather short (15 cm), only intense lightning whistlers with sufficient amplitude above the background noise level may be detected by VLFR. Another reason may be due to the penetration loss of lightning whistlers during the course of the propagation in the ionosphere.

By utilizing VLFR data, we have a great opportunity to study the source characteristics of the whistler producing lightning discharges, corresponding electromagnetic wave propagation, and the effects on the overlaying ionospheric properties. For example, the electrical properties and discharge types of causative lightning discharges can be clarified with the aid of photometric observations. Using the electromagnetic wave data obtained by the DEMETER satellite, Fiser *et al.* [2010] quantitatively compared the detected whistler amplitudes with the distance between the magnetic footprint of the satellite and the source lightning location and with the source lightning currents. Using the electric field data measured by VEFI on board the C/NOFS satellite, Jacobson *et al.* [2011] analyzed the propagation characteristics of lightning whistlers detected in the low magnetic latitudes and showed that the majority of the detected whistlers are relatively simple oblique electron whistlers. On the basis of the detailed data analysis using the VEFI and WWLLN data, Holzworth *et al.* [2011] also presented direct evidence for the relation between lightning discharges and strong whistlers inside equatorial ionospheric density depletions. Similar quantitative analysis can be performed using JEM-GLIMS VLFR

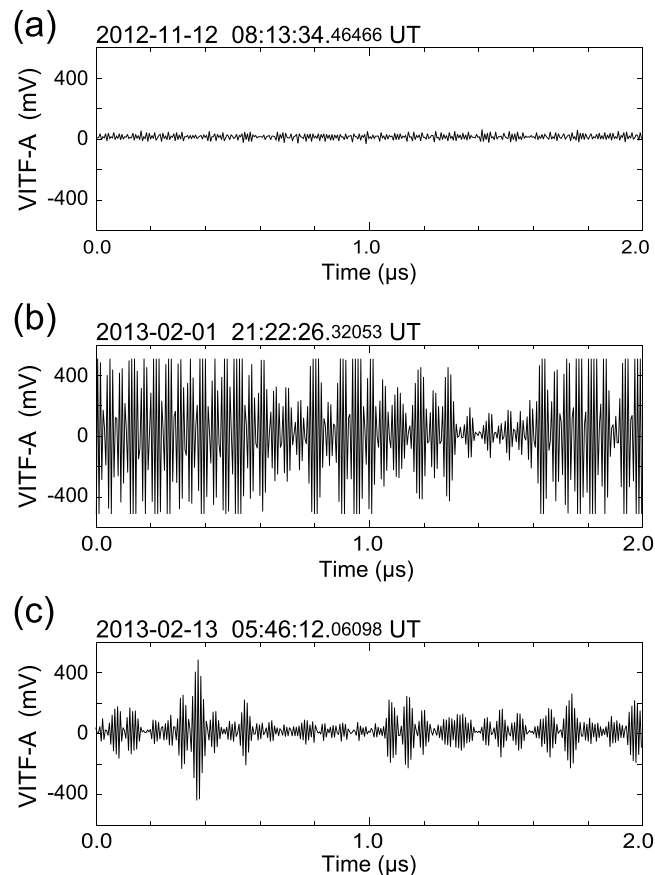


Figure 19. Examples of the VHF waveform data obtained with the VITF A unit. (a) VHF waveform data detected over the Pacific Ocean at 08:13:34.46466 UT on 12 November 2012. The amplitude of this waveform corresponds to the background noise level in the frequency range 70–100 MHz at the ISS. (b) Same as Figure 19a except that the waveform data were detected over China at 21:22:26.32053 UT on 1 February 2013. The multiple pulses are related to the VHF signals generated by urban activities. (c) Lightning-associated VHF pulses measured over Brazil at 05:46:12.06098 UT on 13 February 2013.

data and ground-based lightning measurement data. One advantage of the JEM-GLIMS mission over past satellite missions is that the detailed discharge processes of the parent lightning discharges can be identified using the JEM-GLIMS optical data. The propagation characteristics of VLF waves through the ionosphere over the active thunderstorm regions can be investigated as well. In this case, the electron density in the lower ionosphere can be significantly modified through the heating-ionization process due to intensive discharges and/or TLEs. Moreover, fractional hop whistlers have a significantly small dispersion compared with the majority of magnetospheric whistlers crossing the magnetic equator [Hobara and Hayakawa, 2012]. Nevertheless, the measurable dispersion of fractional hop whistlers will be used to probe high-altitude ionospheric properties, as high electron density in the *F* region makes a significant contribution to whistler dispersion, especially at low latitude where most lightning discharges occur. Finally, as quantitatively analyzed by Lefeuvre *et al.* [2009], identifying the electrical properties of the lightning discharges producing both TLEs and lightning whistlers and clarifying the ionospheric condition in such cases using JEM-GLIMS data is important.

6.2. VHF Pulses From Lightning Discharges

JEM-GLIMS is the first mission to conduct scientific measurements of electromagnetic waves in the VHF range at the ISS. Thus, the background noise levels in the 70–100 MHz frequency range, which is the frequency range of VITF, were not clear. After the first JEM-GLIMS observations, VITF data were carefully analyzed to study the characteristics of detected VHF waveforms and the possible sources of the VHF waves. Figure 19 shows an example of VHF waveform data obtained by the VITF A unit. Figure 19a corresponds to the VITF data obtained at 08:13:34.46466 UT on 12 November 2012. At this time, the ISS was located at 115.841°W, 42.475°S over the Pacific Ocean. From WWLLN data, no lightning activity was confirmed within the FOV of

VITF when such waveform data were obtained. Thus, the waveform in Figure 19a possibly corresponds to the background noise waveform in the 70–100 MHz frequency range at the ISS. The waveform data in Figure 19b were recorded at 21:22:26.32053 UT on 1 February 2013, when the ISS was located at 106.192°E, 33.544°N near Hanzhong City, China. WWLLN lightning data also confirmed that no lightning activity was present within the FOV of VITF when this waveform was recorded. However, the waveform data in Figure 19c were detected at 05:46:12.06098 UT on 13 February 2013, when the ISS was located at 43.725°W, 2.964°S near the east coast of Brazil. In this event, lightning optical emissions were measured by both LSI and PH. As seen in Figures 19b and 19c, these waveforms exhibit quite different characteristics, i.e., the VHF waveform in Figure 19b is a continuous pulse chain with amplitudes exceeding the saturation level, whereas the waveform in Figure 19c has an intermittent wave packet structure. Thus, we concluded that the waveform in Figure 19b is related to the VHF signals generated by urban activities, which is noise for the JEM-GLIMS VITF measurements, and that the VHF waveform in Figure 19c is closely related to the lightning discharges.

Figure 20 is an example of an event where both optical and VHF pulses were simultaneously measured. In this event, the transient optical flash of the lightning discharge was detected by PH at 14:50:30.18751 UT on 25 May 2013. The location of the ISS at this time was 117.237°E, 3.755°N over Borneo Island, Indonesia. Figure 20a shows four consecutive image data of LSI-1 obtained from one frame before the trigger time. In this event, faint optical emissions of the lightning discharge started at the second frame; then, the optical emission grew and moved to the upper right direction at the third and the last frame. The horizontal scale of this emission was found to be ~ 20 km, according to the scale shown in the last frame image. Figure 20b is a plot of the light curve data obtained by PH4 at 512 ms time intervals. As shown in this figure, a strong impulsive optical emission was observed at $t = 0$ ms, and the following multiple optical pulses were intermittently observed in the time $t = 10$ –150 ms time period. The time variations of these multiple optical pulses in the $t = 50$ –150 ms time period show close similarity to the variations in the IC discharge event shown in Figure 12. Although the impulsive emission at $t = 0$ ms may have been caused by the return stroke, it is likely that the multiple optical pulses are related to in-cloud discharges. At the top of this figure, the time interval when LSI-1 image data were obtained is indicated. It is clear that the optical emissions in LSI-1 images are closely related to the impulsive and the following multiple optical pulses measured by PH4. Figure 20c is the expanded plot of PH4 data for the time interval between $t = 60$ ms and $t = 100$ ms. The multiple emissions in this time period were found to have a repetition period of ~ 3 ms. Figure 20d shows a histogram of the number of VHF data sets acquired by VITF in the $t = 60$ –100 ms time period. As described in section 2.1, when the amplitude of a VHF pulse detected by the VITF A unit exceeds the trigger threshold level, a VHF data set containing the trigger time and waveform data of the VITF A and B units for 2.56 μ s are stored. The number of the recorded VHF data sets in 1 ms was counted and plotted in Figure 20d. Figure 20e shows examples of VHF pulse waveforms measured by the VITF A unit (top) and B unit (bottom). Note that each panel in this figure corresponds to the waveform data in one VHF data set. From left to right, each data set was recorded at $t = 62.548$, 80.045, and 98.575 ms, respectively.

By comparing Figures 20c and 20d, the variation of the VHF data sets apparently increased with the optical intensity measured by PH4. To clarify the relation between the PH4 intensity variation and the variation of the VHF data sets, cross-correlation analysis was performed. The red solid line in Figure 21a shows the light curve data of PH4, which is the same as that in Figure 20c. Each bar in this figure corresponds to the 1 ms average value of the PH4 intensities. Figures 21b and 20d are the same. Using the 1 ms time resolution data in Figures 21a and 21b, a cross-correlation function was calculated. Figure 21c shows a plot of the cross-correlation function between the PH4 light curve data and the lagged variation of the VHF data sets as a function of lag δt ms. The cross-correlation function maximum is 0.22 at $\delta t = 1$ ms, where the variation of the VHF data sets was shifted by +1 ms. Hence, the variations of the lightning optical emissions measured by PH4 and the variation of the VHF data sets are weakly correlated.

One of the reasons for the weak correlation may be that VITF detected only intense VHF pulses emitted by lightning discharges detected by the JEM-GLIMS optical instruments. In this event, the trigger threshold level of VITF was set at +452 mV, while the input voltage range of the VITF electronics is ± 512 mV. If VHF pulses with weak amplitudes are also exhaustively recorded, the cross-correlation between the optical intensity variations and the variations of the VHF data sets may improve. Another reason for the weak correlation may be the simultaneous detection of VHF pulses excited by lightning discharges different from the LSI-detecting lightning discharges in Figure 20a. If only the VHF pulses generated by the LIS-detecting lightning discharges are selected from the VITF data, the cross-correlation may improve. Thus, the source locations of the VHF pulses

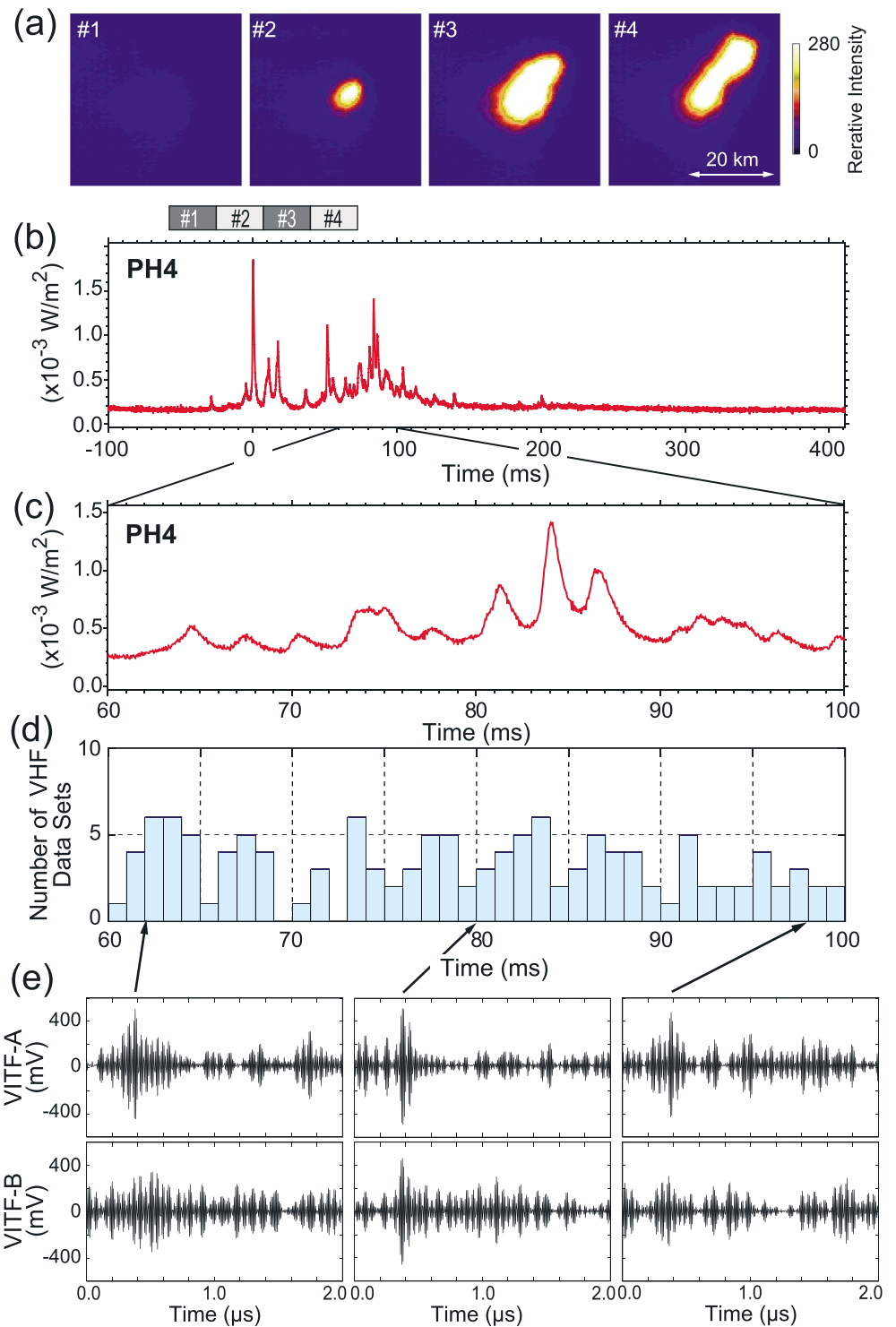


Figure 20. Example of the VHF pulse event detected by VITF. The event trigger time stamped by PH is 14:50:30.18751 UT on 25 May 2013. (a) Four consecutive images of lightning emissions measured by LSI-1. (b) Light curve data obtained by PH4 for the 512 ms time interval. (c) Same as Figure 20b except for the time interval of $t = 60\text{--}100$ ms. (d) Histogram of the detection number of VHF data sets. (e) Examples of VHF pulse waveforms. Note that the waveform data in each panel correspond to one VHF data set. Top and bottom panels show the waveform observed by the VITF A unit and B unit, respectively. From left to right, each data set was recorded at $t = 62.548, 80.045,$ and 98.575 ms, respectively.

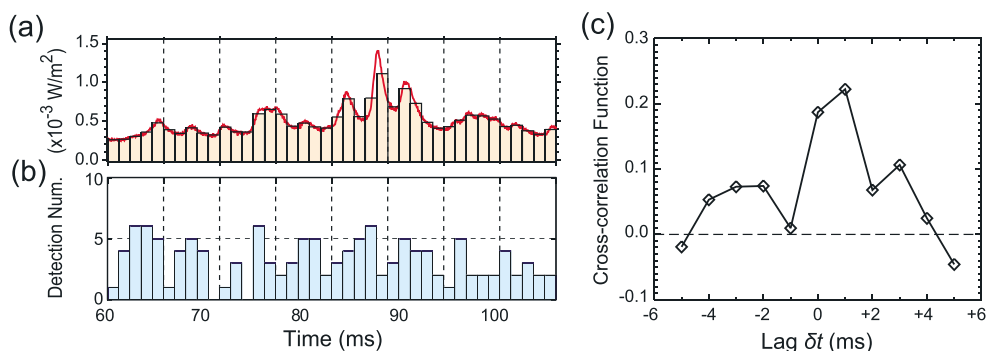


Figure 21. Results of the cross-correlation analysis between the PH4 light curve data and the variation of the VHF data sets for the event presented in Figure 20. (a) PH4 light curve data for the time interval between $t = 60$ and 100 ms. Each bar corresponds to the 1 ms average value of the PH4 intensities. (b) Same as Figure 20d. (c) Cross-correlation function between the PH4 light curve data and the lagged variation of the VHF data sets.

must be identified. Using the waveform data of VHF pulses shown in Figure 20e and an analysis method based on the interferometric technique, it is possible to estimate the source locations of the VHF pulses in the thundercloud. In fact, such a data analysis technique has already been developed, and we succeeded in estimating the source locations [Morimoto *et al.*, 2014; Kikuchi *et al.*, 2014]. In the same manner as ground-based VHF interferometers (e.g., LMA developed in the United States [Thomas *et al.*, 2000, 2004; Goodman *et al.*, 2005] and VHF Broadband Digital Interferometry System developed by Osaka University), it is possible to estimate the spatiotemporal evolution of the lightning currents and of the TLE-exciting lightning currents in a thundercloud, which will essentially contribute to the understanding of the EMP effects of horizontal lightning currents in thunderclouds on the creation of plasma irregularities at the ionospheric *D* region and to the identification of the occurrence conditions of TLEs.

In contrast, it can also be deduced that the weak cross correlation between the optical intensity variations and the variations of the VHF data sets in Figure 21 is natural. As reported by Jacobson and Light [2012], the optical intensities of intracloud discharges producing narrow bipolar events (NBEs) are inversely proportional to the radiated electromagnetic power of NBEs. In that report, NBEs are suggested to be generally related to intense VHF pulse signals. Thus, observing a weak correlation between the PH4 light curve data and the variations of the VHF data sets in Figure 21 is obvious though it is moot whether the VHF pulses detected by VITF are related to NBEs.

Nevertheless, the comparison of Figure 19 and Figure 20 for the first time reveals that the VHF pulses observed by VITF are likely to be excited by lightning discharges measured by the JEM-GLIMS optical instruments and are possibly related to in-cloud discharge currents or the subsequent return stroke.

7. Conclusion

JEM-GLIMS is currently continuing the stable orbital observations of lightning discharges and TLEs that started in November 2012. Till the end of January 2014, a total of 3131 lightning events had been detected by the optical instruments and electromagnetic receivers. The global distribution of the detected lightning events clearly shows that most of the events were detected over continental regions, that is, over Central Africa, North and South America, and Southeast Asia. In addition, the clear seasonal variations in detected lightning events were also confirmed, and these events were centered over continental regions in the respective summer hemisphere. Although the distribution derived from JEM-GLIMS data has not yet been converted into occurrence rate (unit: events/km²/month), it is a comparable result to that derived from the measurements of MicroLab-1/OTD and TRMM/LIS.

Based on the imaging and photometric nadir observations of JEM-GLIMS, it becomes possible to not only measure morphological and spatiotemporal changes of lightning optical emissions but also characterize the detailed processes of lightning discharges especially from the nadir PH observations, as the effects of the atmospheric transmission from the light source to the observer can be minimized in nadir observations compared with limb observations. JEM-GLIMS has succeeded in detecting the transient optical emissions accompanying FUV emissions, which strongly imply the occurrence of TLEs, because FUV emissions from the

ground level must be perfectly absorbed by atmospheric O₃ and O₂. In some of these events, no significant optical emission was measured in LSI-2 images, suggesting the occurrence of elves, not sprites. The events containing FUV signals are distributed over continental and oceanic regions. As the occurrence ratio of elves over the oceanic region is higher than that over the land region [Chen *et al.*, 2008] and as intense –CG discharges with high peak currents tend to occur over the oceanic region [Füllekrug *et al.*, 2002], FUV events without LSI-2 emissions occurring over the oceanic regions are likely to be associated with elves events.

JEM-GLIMS has succeeded in detecting lightning whistlers and VHF pulses excited by lightning discharges. For lightning whistlers, the waveform and dynamic spectrum show a clear falling-tone frequency dispersion appearing from $f = 30$ kHz to $f = 2$ kHz, which is a typical characteristic of fractional hop whistlers. From the calculation of the group velocity of plasma waves in the VLF range in the ionosphere, the observed time delay of the whistler from the detection time of the parent lightning discharge by PH is found to be consistent with the calculated time delay. Using such VLFR data, it is expected that the electrical properties of the lightning discharges exciting whistlers and the ionospheric conditions permitting the penetration of VLF waves into the ionosphere can be clarified. VITF conducted the first interferometric observations of electromagnetic waves emitted by lightning discharges and succeeded in detecting VHF pulses with JEM-GLIMS optical measurements. It was observed for the first time that VHF pulses are likely to be excited by the lightning discharges measured by the JEM-GLIMS optical instruments and are possibly related to in-cloud discharge currents or the subsequent return stroke, based on simultaneous measurements by the JEM-GLIMS optical instruments and electromagnetic wave receivers. From these pulse data and the interferometric analysis, it is possible to estimate the source locations of VHF pulses.

Finally, detailed comparisons between JEM-GLIMS optical and electromagnetic waveform data and ground-based lightning observation data will enable us to clarify the occurrence conditions of sprites, which is the main goal of the JEM-GLIMS mission. To achieve this, we have developed data processing techniques to identify the type of TLEs: (1) a subtraction of the appropriately scaled LSI-1 image from LSI-2 image, (2) a calculation of the intensity ratio between different PH channels, and (3) an estimation of the polarization and CMC for the parent CG discharges of the event [Sato *et al.*, 2013]. From a synthetic comparison of these results, we have succeeded in distinguishing the types of the observed TLEs [Sato *et al.*, 2013, 2014]. We also expect that more precise global occurrence rates and the distributions of TLEs and their LT dependences can be estimated, and the derived results will lead us to the quantitative estimation of the global chemical impact of TLEs on Earth's atmosphere. In addition, it is expected that the first quantitative latitudinal dependences of the IC/CG ratio (Z value) can be estimated on the basis of the JEM-GLIMS imaging and photometric observations characterizing the discharge processes of lightning and that the global occurrence distributions and rates of whistlers and VHF pulses and their LT dependences can also be estimated. The detailed presentations of all these results are beyond the scope of this paper and will be summarized in future papers.

Acknowledgments

This work was supported by JSPS KAKENHI Grant-in-Aid for Scientific Research (B) 24340117 and MEXT KAKENHI Grant-in-Aid for Specially Promoted Research 19002002. This work complies with the AGU data policy; JEM-GLIMS and Syowa ELF data presented in this study are available upon request from the corresponding author, Mitsuteru Sato (msato@ep.sci.hokudai.ac.jp). All data analyses were performed using the Interactive Data Language (IDL) version 8.2. The authors thank AD Co., Ltd., YuCALY Optics Co., Ltd., Meisei Electric Co., Ltd., Dainichi Denshi Co., Ltd., Advanced Engineering Services Co., Ltd., Japan Communication Equipment Co., Ltd., Kawasaki Technology Co., Ltd., and IHI Aerospace Co., Ltd for the development of the JEM-GLIMS systems. The authors acknowledge JAXA's full support for the JEM-GLIMS continuous operation and data acquisition. We wish to thank the party of Japanese Antarctic Research Expedition (JARE) and National Institute of Polar Research (NIPR) for the continuous support of ELF observations at Syowa station in Antarctica. The authors thank Yoav Yair and two other anonymous reviewers for their comments and suggestions for improving this paper.

References

- Adachi, T., H. Fukunishi, Y. Takahashi, and M. Sato (2004), Roles of the EMP and QE field in the generation of columniform sprites, *Geophys. Res. Lett.*, *31*, L04107, doi:10.1029/2003GL019081.
- Adachi, T., et al. (2008), Electric fields and electron energies in sprites and temporal evolutions of lightning charge moment measurements, *J. Phys. D: Appl. Phys.*, *41*(23), 234010.
- Adachi, T., et al. (2012), Coincident observation of lightning using spaceborne spectrophotometer and ground-level electromagnetic sensors, Abstract AE23B-0330 presented at 2012 Fall Meeting, AGU, San Francisco, Calif., 3–7 Dec.
- Altaratz, O., Z. Levin, Y. Yair, and B. Ziv (2003), Lightning activity over land and sea on the eastern coast of the Mediterranean, *Mon. Weather Rev.*, *131*, 2060–2070.
- Baharudin, Z., N. Ahmad, M. Fernando, V. Cooray, and J. Mäkelä (2012), Comparative study on preliminary breakdown pulse trains observed in Johor, Malaysia and Florida, USA, *Atmos. Res.*, *117*, 111–121, doi:10.1016/j.atmosres.2012.01.012.
- Bell, T., S. Reising, and U. Inan (1998), Intense continuing currents following positive cloud-to-ground lightning associated with red sprites, *Geophys. Res. Lett.*, *25*(8), 1285–1288, doi:10.1029/98GL00734.
- Blanc, E., T. Farges, R. Roche, D. Brebion, T. Hua, A. Labarthe, and V. Melnikov (2004), Nadir observations of sprites from the International Space Station, *J. Geophys. Res.*, *109*, A02306, doi:10.1029/2003JA009972.
- Boccippio, D., E. Williams, S. Heckman, W. Lyons, I. Baker, and R. Boldi (1995), Sprites, ELF transients, and positive ground strokes, *Science*, *269*(5227), 1088–1091, doi:10.1126/science.269.5227.1088.
- Boccippio, D., J. Steven, J. Goodman, and S. Heckman (2000), Regional differences in tropical lightning distributions, *J. Appl. Meteorol.*, *39*, 2231–2248.
- Boccippio, D., K. Cummins, H. Christian, and S. Goodman (2001), Combined satellite and surface-based estimation of the intracloud/cloud-to-ground lightning ratio over the continental United States, *Mon. Weather Rev.*, *129*(1), 108–122.
- Bucselo, E., et al. (2003), N₂ ($B^3\Pi_g$) and N₂⁺ ($A^2\Pi_u$) vibrational distributions observed in sprites, *J. Atmos. Sol. Terr. Phys.*, *65*, 583–590.
- Cecil, D., D. Buechler, and R. Blakeslee (2014), Gridded lightning climatology from TRMM-LIS and OTD: Dataset description, *Atmos. Res.*, *135–136*, 404–414.

- Chang, S. C., C. L. Kuo, L. J. Lee, A. B. Chen, H. T. Su, R. R. Hsu, H. U. Frey, S. B. Mende, Y. Takahashi, and L. C. Lee (2010), ISUAL far-ultraviolet events, elves, and lightning current, *J. Geophys. Res.*, *115*, A00E46, doi:10.1029/2009JA014861.
- Chen, A. B., et al. (2008), Global distributions and occurrence rates of transient luminous events, *J. Geophys. Res.*, *113*, A08306, doi:10.1029/2008JA013101.
- Christian, H. J., et al. (2003), Global frequency and distribution of lightning as observed from space by the Optical Transient Detector, *J. Geophys. Res.*, *108*(D1), 4005, doi:10.1029/2002JD002347.
- Chum, J., O. Santolik, and M. Parrot (2009), Analysis of subprotonospheric whistlers observed by DEMETER: A case study, *J. Geophys. Res.*, *114*, A02307, doi:10.1029/2008JA013585.
- Cummer, S., and M. Füllekrug (2001), Unusually intense continuing current in lightning produces delayed mesospheric breakdown, *Geophys. Res. Lett.*, *28*(3), 495–498.
- Cummer, S., and W. Lyons (2005), Implication of lightning charge moment changes for sprite initiation, *J. Geophys. Res.*, *110*, A04304, doi:10.1029/2004JA010812.
- Fiser, J., J. Chum, G. Diendorfer, M. Parrot, and O. Santolik (2010), Whistler intensities above thunderstorms, *Ann. Geophys.*, *28*, 37–46.
- Franz, R., R. Nemzek, and J. Winckler (1990), Television image of a large upward electrical discharge above a thunderstorm, *Science*, *264*, 48–51.
- Fukunishi, H., Y. Takahashi, M. Kubota, K. Sakanoi, U. Inan, and W. Lyons (1996), Elves: Lightning-induced transient luminous events in the lower ionosphere, *Geophys. Res. Lett.*, *23*, 2157–2160.
- Füllekrug, M., and S. Constable (2000), Global triangulation of intense lightning discharges, *Geophys. Res. Lett.*, *27*(3), 333–336.
- Füllekrug, M., C. Price, Y. Yair, and E. R. Williams (2002), Intense oceanic lightning, *Ann. Geophys.*, *20*, 133–137.
- Gamerota, W., S. Cummer, J. Li, H. Stenbaek-Nielsen, R. Haaland, and M. McHarg (2011), Comparison of sprite initiation altitudes between observations and models, *J. Geophys. Res.*, *116*, A02317, doi:10.1029/2010JA016095.
- Goodman, S., et al. (2005), The North Alabama lightning mapping array: Recent severe storm observations and future prospects, *Atmos. Res.*, *76*, 423–437, doi:10.1016/j.atmosres.2004.11.035.
- Gordillo-Vázquez, F. J., A. Luque, and M. Simek (2011), Spectrum of sprite halos, *J. Geophys. Res.*, *116*, A09319, doi:10.1029/2011JA016652.
- Greenberg, E., C. Price, Y. Yair, M. Ganot, J. Bór, and G. Satori (2007), ELF transients associated with sprites and elves in eastern Mediterranean winter thunderstorms, *J. Atmos. Sol. Terr. Phys.*, *69*, 1569–1586.
- Helliwell, R. A. (1965), *Whistlers and Related Ionospheric Phenomena*, 349 pp., Stanford Univ. Press, Stanford, Calif.
- Hiraki, Y., Y. Kasai, and H. Fukunishi (2008), Chemistry of sprite discharges through ion-neutral reactions, *Atmos. Chem. Phys.*, *8*, 3919–3928.
- Hobara, Y., and M. Hayakawa (2012), The effects of lightning on the ionosphere/magnetosphere, in *Lightning Electromagnetics*, edited by V. Cooray, pp. 647–685, IET Power and energy, London.
- Holzworth, R., M. McCarthy, R. Pfaff, A. Jacobson, W. Willcockson, and D. Rowland (2011), Lightning-generated whistler waves observed by probes on the Communication/Navigation Outage Forecast System satellite at low latitudes, *J. Geophys. Res.*, *116*, A06306, doi:10.1029/2010JA016198.
- Hu, W., S. Cummer, and W. Lyons (2007), Testing sprite initiation theory using lightning measurements and modeled electromagnetic fields, *J. Geophys. Res.*, *112*, D13115, doi:10.1029/2006JD007939.
- Ignaccolo, M., T. Farges, A. Mika, T. H. Allin, O. Chanrion, E. Blanc, T. Neubert, A. C. Fraser-Smith, and M. Füllekrug (2006), The planetary rate of sprite events, *Geophys. Res. Lett.*, *33*, L11808, doi:10.1029/2005GL025502.
- Jacobson, A., and T. Light (2012), Revisiting “Narrow Bipolar Event” intracloud lightning using the FORTE satellite, *Ann. Geophys.*, *30*, 389–404, doi:10.5194/angeo-30-389-2012.
- Jacobson, A., R. Holzworth, R. Pfaff, and M. McCarthy (2011), Study of oblique whistlers in the low-latitude ionosphere, jointly with the C/NOFS satellite and the World-Wide Lightning Location Network, *Ann. Geophys.*, *29*, 851–863, doi:10.5194/angeo-29-851-2011.
- Jehl, A., T. Farges, and E. Blanc (2013), Color pictures of sprites from nondedicated observation on board the International Space Station, *J. Geophys. Res. Space Physics*, *118*, 454–461, doi:10.1029/2012JA018144.
- Kikuchi, H., S. Yoshida, T. Morimoto, T. Ushio, and Z.-I. Kawasaki (2011), Satellite observation for lightning discharges and analysis of VHF electromagnetic waveforms, *IEEJ Trans. Fundam. Mater.*, *131*(9), 705–710, doi:10.1541/ieejfms.131.705.
- Kikuchi, H., S. Yoshida, T. Morimoto, T. Ushio, and Z.-I. Kawasaki (2013), VHF radio wave observations by Mado-1 satellite and evaluation of its relationship with lightning discharges, *IEICE Trans. Commun.*, *E96-B*, 880–886, doi:10.1587/transcom.E96.B.880.
- Kikuchi, H., T. Morimoto, T. Ushio, M. Sato, A. Yamazaki, and M. Suzuki (2014), Lightning observations using VHF interferometer installed on the International Space Station, Abstract AS28-D1-AM2-ED003 presented at AOGS 2014, Sapporo, 28 July–1 Aug.
- Kikuchi, M., et al. (2011), Development of science data handling unit (SHU) for Global Lightning And Sprite Measurements (GLIMS) onboard Japanese experiment module (JEM) of ISS, *IEEJ Trans. Fundam. Mater.*, *131*(12), 989–993, doi:10.1541/ieejfms.131.989.
- Kotroni, V., and K. Lagouvardos (2008), Lightning occurrence in relation with elevation, terrain slope, and vegetation cover in the Mediterranean, *J. Geophys. Res.*, *113*, D21118, doi:10.1029/2008JD010605.
- Kuo, C.-L., R. R. Hsu, A. B. Chen, H. T. Su, L. C. Lee, S. B. Mende, H. U. Frey, H. Fukunishi, and Y. Takahashi (2005a), Electric fields and electron energies inferred from the ISUAL recorded sprites, *Geophys. Res. Lett.*, *32*, L19103, doi:10.1029/2005GL023389.
- Kuo, C.-L., B. Chen, R. Hsu, H. Su, L. Lee, S. Mende, H. Frey, H. Fukunishi, and Y. Takahashi (2005b), Elves spectrum based on the ISUAL photometric data, *Eos Trans. AGU*, *86*(52), Fall Meet. Suppl., Abstract AE23A-0994.
- Kuo, C.-L., et al. (2007), Modeling elves observed by FORMOSAT-2 satellite, *J. Geophys. Res.*, *112*, A11312, doi:10.1029/2007JA012407.
- Lang, T., J. Li, W. Lyons, S. Cummer, S. Rutledge, and D. MacGorman (2011), Transient luminous events above two mesoscale convective systems: Charge moment change analysis, *J. Geophys. Res.*, *116*, A10306, doi:10.1029/2011JA016758.
- Lefeuvre, F., R. Marshall, J. Pinçon, U. Inan, D. Lagoutte, M. Parrot, and J. Berthelier (2009), On remote sensing of transient luminous events’ parent lightning discharges by ELF/VLF wave measurements on board a satellite, *J. Geophys. Res.*, *114*, A09303, doi:10.1029/2009JA014154.
- Li, J., S. Cummer, W. Lyons, and T. Nelson (2008), Coordinated analysis of delayed sprites with high-speed images and remote electromagnetic fields, *J. Geophys. Res.*, *113*, D20206, doi:10.1029/2008JD010008.
- Liu, C., and E. Zipser (2008), Diurnal cycles of precipitation, clouds, and lightning in the tropics from 9 years of TRMM observations, *Geophys. Res. Lett.*, *35*, L04819, doi:10.1029/2007GL032437.
- Lu, G., S. Cummer, J. Li, F. Han, R. Blakeslee, and H. Christian (2009), Charge transfer and in-cloud structure of large-charge-moment positive lightning strokes in a mesoscale convective system, *Geophys. Res. Lett.*, *36*, L15805, doi:10.1029/2009GL038880.
- Lu, G., et al. (2013), Coordinated observations of sprites and in-cloud lightning flash structure, *J. Geophys. Res.*, *118*, 6607–6632, doi:10.1002/jgrd.50459.
- Lyons, W. (1996), Sprite observations above the U.S. high plains in relation to their parent thunderstorm systems, *J. Geophys. Res.*, *101*, 29,641–29,652.
- Mackerras, D., and M. Darveniza (1994), Latitudinal variation of lightning occurrence characteristics, *J. Geophys. Res.*, *99*(D5), 10,813–10,821.

- Mackerras, D., M. Darveniza, R. Orville, E. Williams, and S. Goodman (1998), Global lightning: Total, cloud and ground flash estimates, *J. Geophys. Res.*, *103*, 19,791–19,809.
- Maeda, K., and I. Kimura (1984), *Gendai Denji Hado Ron*, 248 pp., Omusha, Tokyo.
- Marshall, R., U. Inan, and V. Glukhov (2010), Elves and associated electron density changes due to cloud-to-ground and in-cloud lightning discharges, *J. Geophys. Res.*, *115*, A00E17, doi:10.1029/2009JA014469.
- Morimoto, T., Z.-I. Kawasaki, and T. Ushio (2005), Lightning observations and consideration of positive charge distribution inside thunderclouds using VHF broadband digital interferometry, *Atmos. Res.*, *76*, 445–454, doi:10.1016/j.atmosres.2004.11.024.
- Morimoto, T., H. Kikuchi, M. Sato, M. Suzuki, A. Yamazaki, and T. Ushio (2011), VHF lightning observations on JEM-GLIMS mission: Gradual approach to realize space-borne VHF broadband digital interferometer, *IEEJ Trans. Fundam. Mater.*, *131*(12), 977–982, doi:10.1541/ieefms.131.977.
- Morimoto, T., H. Kikuchi, T. Ushio, Z.-I. Kawasaki, M. Sato, A. Yamazaki, and M. Suzuki (2014), VHF lightning observations by digital interferometry from ISS/JEM-GLIMS, Abstract O-12-06 presented at Int. Conf. on Atmos. Electr., Oklahoma, 16–20 June.
- Mushtak, V., E. Williams, and D. Boccippio (2005), Latitudinal variations of cloud base height and lightning parameters in the tropics, *Atmos. Res.*, *76*, 222–230, doi:10.1016/j.atmosres.2004.11.010.
- Nag, A., and V. Rakov (2008), Pulse trains that are characteristic of preliminary breakdown in cloud-to-ground lightning but are not followed by return stroke pulses, *J. Geophys. Res.*, *113*, D01102, doi:10.1029/2007JD008489.
- Nagano, I., S. Yagitani, K. Miyamura, and S. Makino (2003), Full-wave analysis of elves created by lightning-generated electromagnetic pulses, *J. Atmos. Sol. Terr. Phys.*, *65*, 615–625.
- Nickolaenko, A. P., and M. Hayakawa (2002), *Resonances in the Earth-Ionosphere Cavity*, pp. 177–182, Kluwer Acad., Dordrecht, Netherlands.
- Ohkubo, A., H. Fukunishi, Y. Takahashi, and T. Adachi (2005), VLF/ELF spheric evidence for in-cloud discharge activity producing sprites, *Geophys. Res. Lett.*, *32*, L04812, doi:10.1029/2004GL021943.
- Orville, R., and R. Henderson (1984), Absolute spectral irradiance measurements of lightning from 375 to 880 nm, *J. Atmos. Sci.*, *41*(21), 3180–3187.
- Parrot, M., J. Sauvaud, S. Soula, J. Pinçon, and O. van der Velde (2013), Ionospheric density perturbations recorded by DEMETER above intense thunderstorms, *J. Geophys. Res. Space Physics*, *118*, 5169–5176, doi:10.1002/jgra.50460.
- Pasko, V. P., U. S. Inan, T. F. Bell, and Y. N. Taranenko (1997), Sprites produced by quasi-electrostatic heating and ionization in the lower ionosphere, *J. Geophys. Res.*, *102*, 4529–4561, doi:10.1029/96JA03528.
- Pasko, V., M. Stanley, J. Matthews, U. Inan, and T. Wood (2002), Electrical discharge from a thundercloud top to the lower ionosphere, *Nature*, *416*, 152–154, doi:10.1038/416152a.
- Prentice, S., and D. Mackerras (1977), The ratio of the cloud to cloud-ground lightning flashes in thunderstorms, *J. Appl. Meteorol.*, *16*, 545–550.
- Price, C., and B. Federmesser (2006), Lightning-rainfall relationships in Mediterranean winter thunderstorms, *Geophys. Res. Lett.*, *33*, L07813, doi:10.1029/2005GL024794.
- Qin, J., S. Celestin, and V. P. Pasko (2011), On the inception of streamers from sprite halo events produced by lightning discharges with positive and negative polarity, *J. Geophys. Res.*, *116*, A06305, doi:10.1029/2010JA016366.
- Qin, J., S. Celestin, V. Pasko, S. Cummer, M. McHarg, and H. Stenbaek-Nielsen (2013), Mechanism of column and carrot sprites derived from optical and radio observations, *Geophys. Res. Lett.*, *40*, 4777–4782, doi:10.1002/grl.50910.
- Rakov, V. A., and M. A. Uman (2003), *Lightning: Physics and Effects*, 687 pp., Cambridge Univ. Press, Cambridge, U. K.
- Rison, W., R. Thomas, P. Krehbiel, T. Hamlin, and J. Harlin (1999), A GPS-based three-dimensional lightning mapping system: Initial observations in central New Mexico, *Geophys. Res. Lett.*, *26*(23), 3573–3576.
- Sato, M., and H. Fukunishi (2003), Global sprite occurrence locations and rates derived from triangulation of transient Schumann resonance events, *Geophys. Res. Lett.*, *30*(16), 1859, doi:10.1029/2003GL017291.
- Sato, M., Y. Takahashi, A. Yoshida, and T. Adachi (2008), Global distribution of intense lightning discharges and their seasonal variations, *J. Phys. D: Appl. Phys.*, *41*, 234011.
- Sato, M., Y. Takahashi, M. Kikuchi, M. Suzuki, A. Yamazaki, and T. Ushio (2011a), Lightning and Sprite Imager (LSI) onboard JEM-GLIMS, *IEEJ Trans. Fundam. Mater.*, *131*(12), 994–999, doi:10.1541/ieefms.131.994.
- Sato, M., Y. Takahashi, M. Suzuki, A. Yamazaki, and T. Ushio (2011b), Six-channel spectrophotometers (PH) onboard JEM-GLIMS, *IEEJ Trans. Fundam. Mater.*, *131*(12), 1000–1005, doi:10.1541/ieefms.131.1000.
- Sato, M., et al. (2013), Photometric characteristics of sprites and elves derived from JEM-GLIMS nadir observations, Abstract AE32A-03 presented at 2013 Fall Meeting, AGU, San Francisco, Calif., 9–13 Dec.
- Sato, M., T. Adachi, M. Mihara, T. Ushio, T. Morimoto, H. Kikuchi, M. Suzuki, A. Yamazaki, and Y. Takahashi (2014), Spatiotemporal characteristics of sprites and sprite-related VHF signals measured by JEM-GLIMS, Abstract AE31B-3412 presented at 2014 Fall Meeting, AGU, San Francisco, Calif., 15–19 Dec.
- Sentman, D., E. Wescott, D. Osborne, D. Hampton, and M. Heavner (1995), Preliminary results of the sprites94 aircraft campaign: Red sprites, *Geophys. Res. Lett.*, *22*, 1205–1208.
- Sentman, D., E. M. Wescott, R. H. Picard, H. C. Stenbaek-Nielsen, E. M. Dewan, D. R. Moudry, F. T. Sabbas, M. J. Heavner, and J. Morrill (2003), Simultaneous observations of mesospheric gravity waves and sprites generated by a midwestern thunderstorm, *J. Atmos. Sol. Terr. Phys.*, *65*, 537–550.
- Sentman, D., H. Stenbaek-Nielsen, M. McHarg, and J. Morrill (2008), Plasma chemistry of sprite streamers, *J. Geophys. Res.*, *113*, D11112, doi:10.1029/2007JD008941.
- Sharma, S., M. Fernando, and C. Gomes (2005), Signatures of electric field pulses generated by cloud flashes, *J. Atmos. Sol. Terr. Phys.*, *67*, 413–422.
- Smith, R., and J. Angerami (1968), Magnetospheric properties deduced fromOGO 1 observations of ducted and nonducted whistlers, *J. Geophys. Res.*, *73*, 1–20.
- Su, H. T., R. R. Hsu, A. B. Chen, Y. C. Wang, W. S. Hsiao, W. C. Lai, L. C. Lee, M. Sato, and H. Fukunishi (2003), Gigantic jets between a thundercloud and the ionosphere, *Nature*, *423*, 974–976, doi:10.1038/nature01759.
- Suszcynsky, D., M. W. Kirkland, A. R. Jacobson, R. C. Franz, S. O. Knox, J. L. L. Guillen, and J. L. Green (2000), FORTE observations of simultaneous VHF and optical emissions from lightning: Basic phenomenology, *J. Geophys. Res.*, *105*(D2), 2191–2201.
- Thomas, R., P. R. Krehbiel, W. Rison, T. Hamlin, D. J. Boccippio, S. J. Goodman, and H. J. Christian (2000), Comparison of ground-based 3-dimensional lightning mapping observations with satellite-based LIS observations in Oklahoma, *Geophys. Res. Lett.*, *27*(12), 1703–1706.
- Thomas, R., P. Krehbiel, W. Rison, S. Hunyady, W. Winn, T. Hamlin, and J. Harlin (2004), Accuracy of the lightning mapping array, *J. Geophys. Res.*, *109*, D14207, doi:10.1029/2004JD004549.
- Ushio, T., S. Heckman, K. Driscoll, D. Boccippio, H. Christian, and Z.-I. Kawasaki (2002), Cross-sensor comparison of the Lightning Imaging Sensor (LIS), *Int. J. Remote Sens.*, *23*, 2703–2712.

- Ushio, T., et al. (2011), The Global Lightning And Sprite Measurement (GLIMS) mission of the international space station: Concept and overview, *IEEJ Trans. Fundam. Mater.*, 131(12), 971–976, doi:10.1541/ieejfms.131.971.
- Vadislavsky, E., Y. Yair, C. Erlick, C. Price, E. Greenberg, R. Yaniv, B. Ziv, N. Reicher, and A. Devir (2009), Indication for circular organization of column sprite elements associated with eastern Mediterranean winter thunderstorms, *J. Atmos. Sol. Terr. Phys.*, 71, 1835–1839, doi:10.1016/j.jastp.2009.07.001.
- Wescott, E., D. Sentman, D. Osborne, D. Hampton, and M. Heavner (1995), Preliminary results from the Sprites94 aircraft campaign: 2. Blue jets, *Geophys. Res. Lett.*, 22, 1209–1212.
- Wescott, E., H. Stenbaek-Nielsen, D. Sentman, M. Heavner, D. Moudry, and F. São-Sabbas (2001), Triangulation of sprites, associated halos and their possible relation to causative lightning and micro-meteors, *J. Geophys. Res.*, 106(A6), 10,467–10,478, doi:10.1029/2000JA000182.
- Yair, Y., P. Israelevich, A. D. Devir, M. Moalem, C. Price, J. H. Joseph, Z. Levin, B. Ziv, A. Sternlieb, and A. Teller (2004), New observations of sprites from the space shuttle, *J. Geophys. Res.*, 109, D15201, doi:10.1029/2003JD004497.
- Yair, Y., C. Price, M. Ganot, E. Greenberg, R. Yaniv, B. Ziv, Y. Sherez, A. Devir, J. Bór, and G. Satori (2009), Optical observations of transient luminous events associated with winter thunderstorms near the coast of Israel, *Atmos. Res.*, 91, 529–537, doi:10.1016/j.atmosres.2008.06.018.
- Yair, Y., L. Rubanenko, K. Mezuman, G. Elhalel, M. Pariente, M. Glickman-Pariente, B. Ziv, Y. Takahashi, and T. Inoue (2013), New color images of transient luminous events from dedicated observations on the international space station, *J. Atmos. Sol. Terr. Phys.*, 102, 140–147.